J Mater Sci: Mater Electron (2025) 36:1925

Optical limiting and third-order nonlinear optical properties of a novel thiazole-based organic NLO material for optoelectronic applications: experimental and theoretical insights

V. Keerthikumara[1], H. Keshav Kumar[1], M. Vindu Vahini[4], H. M. Bhanu Prakash[1], N. R. Bhavya[1,2], Samyukta Ram Mohan[1], Tejaswi Ashok Hegde[3], and M. Mahendra[1,*]

[1] *Department of Studies in Physics, University of Mysore, Manasagangotri, Mysuru, Karnataka 570006, India*
[2] *Department of Physics, Vidyavardhaka College of Engineering, Mysuru, Karnataka 570002, India*
[3] *Department of Physics, Hindustan Institute of Technology and Science, Chennai 603103, India*
[4] *Department of Physics, Maharani's Science College for Women (Autonomous), Mysuru, Karnataka 570005, India*

Received: 23 July 2025
Accepted: 12 October 2025

ABSTRACT

A novel organic nonlinear optical (NLO) material, (E)-N′-(4-methylthiazol-5-yl) methylenebenzohydrazide (MMB), was synthesized via a reflux method and thoroughly characterized using single-crystal X-ray diffraction, NMR spectroscopy, and other experimental techniques. The UV–Vis absorption spectrum across various solvents exhibited strong peaks in the 270 to 480 nm range, demonstrating potential for optoelectronic applications. MMB displayed significant NLO responses, with solvent-dependent values for α_{CT}, β_{CT}, and γ_{CT}, emphasizing its adaptability in diverse environments. Thermogravimetric analysis revealed thermal stability up to 188.82℃. Z-scan measurements using a CW laser determined a third-order nonlinear susceptibility ($\chi^{(3)}$) of 3.06×10^{-8} e.s.u., along with optical limiting behavior at a threshold of 3.91×10^{3} Wcm^{-2}. Computational studies based on density functional theory (DFT) provided insights into the electronic structure, charge distribution (FMO, NBO), and intermolecular interactions (QTAIM, NCI). Time-dependent Hartree–Fock (TDHF) calculations yielded both static and dynamic NLO parameters, including linear polarizability and first and second hyperpolarizability. Notably, the first hyperpolarizability at 532 nm was 6.36 times greater than that of urea, while the second hyperpolarizability (0.349×10^{-33} e.s.u.) closely matched experimental results in acetonitrile (0.128×10^{-33} e.s.u.). These characterization and nonlinear optical evaluation presented herein establish MMB as a promising candidate for advanced optoelectronic devices, with implications for future advancements in nonlinear optics and photonics.

Address correspondence to E-mail: mahendra@physics.uni-mysore.ac.in

https://doi.org/10.1007/s10854-025-16018-w
Published online: 24 October 2025

1 Introduction

In recent years, third-order nonlinear optical (NLO) materials have attracted a lot of attention because of their wide range of applications in advanced technologies such as optical limiting, optical switching, and three-dimensional optical data storage [1, 2]. This surge in interest has prompted extensive research into the discovery and advancement of novel compounds with elevated NLO susceptibilities. The interaction between delocalized π-electrons and incident electromagnetic fields is significant for nonlinear polarization mechanisms in organic molecules [3]. In the mid-twentieth century, Diels and Alder's pioneering work [4] laid the foundation for the investigation of organic materials with robust NLO responses, establishing fundamental principles in nonlinear optics. Since then, researchers have focused on enhancing these materials' NLO properties by strategically introducing electron-donor and electron-acceptor substituents. This substitution improves polarizability and dipole moment, which are critical factors for improving NLO behaviour [5]. Schiff base ligands have been particularly interesting because of their well-defined structures, which are stabilized by intermolecular forces like hydrogen bonding and π-π stacking [6]. Schiff bases structural attributes make them versatile for various uses, such as in thermoresistant materials and pharmaceuticals [7]. These structural attributes contribute to their wide range of biological applications, including antioxidant, anticonvulsant, antibacterial, and anti-schizophrenia activities [8]. Among Schiff bases, thiazole derivatives stand out because of their excellent pharmacological properties and ability to interact with metal ions, enhancing their therapeutic efficacy [9]. Thiazole compounds, for instance, have demonstrated promising outcomes in anticancer studies, demonstrating potent cytotoxic effects against various cancer cell lines [10], and rendering them attractive candidates for therapeutic applications.

The potential for nonlinear optical applications of Schiff bases containing thiazole motifs has been increasingly highlighted by recent research. Thiazole's distinctive properties, such as its rapid broadband electrical responsiveness and low dielectric constant, make it a promising candidate for optoelectronic applications [11]. Studies have focused on chromophores containing π-conjugated five-membered rings, such as thiazole, pyrazine, and pyrimidine, which frequently act as electron acceptors when paired with electron-donating groups or heterocycles to enhance charge transfer and nonlinear optical (NLO) properties [12]. Fluorescence, solvatochromism, and notable NLO behavior are among the characteristics of these chromophores [13, 14]. Haroon et al. [15] developed thiazole-based materials exhibiting high nonlinear susceptibility, while Roposo et al. [16] synthesized NLO-active chromophores featuring thiazole rings. The structural impact of thiazole on charge transfer, polarization, and donor–acceptor orientation has been increasingly recognized as a crucial factor in enhancing NLO properties [17].

The research on thiazole-based Schiff bases under continuous-wave (CW) laser excitation is still limited, despite the significant progress made in the development of Schiff base derivatives with NLO properties. In particular, the relationship between molecular structure and third-order NLO behaviour is still insufficiently understood through a combined experimental and computational approach. Consequently, the purpose of this investigation is to create and evaluate a novel Schiff base that contains thiazole in order to provide a thorough comprehension of its spectroscopic, nonlinear optical, and structural characteristics, thereby addressing this research gap.

The current work presents a newly synthesized thiazole-based Schiff base, (E)-N′-(4-methylthiazol-5-yl)methylenebenzohydrazide (MMB), intended for improved third-order NLO properties, although earlier research has examined crystal growth, linear optical and structural properties, and pharmacological applications of Schiff base derivatives [18–20]. In contrast to previous studies, this one offers a thorough grasp of the structure–property relationship governing nonlinear optical behaviour by combining experimental Z-scan measurements with DFT simulations. To the best of our knowledge, no prior reports have been made on the synthesis, characterization, and NLO evaluation of this particular compound (MMB) under CW laser excitation.

The synthesized compound (MMB) was fully characterized using single-crystal X-ray diffraction (SC-XRD), NMR spectroscopy (^{13}C and ^{1}H), UV–Vis–NIR spectroscopy, photoluminescence (PL) measurements, solvatochromic analysis, and thermogravimetric-differential analysis (TG–DTA). The Z-scan method was utilized to assess its third-order NLO characteristics. This work offers a thorough understanding of the nonlinear optical behaviour of this thiazole-based Schiff base and illustrates its potential for sophisticated

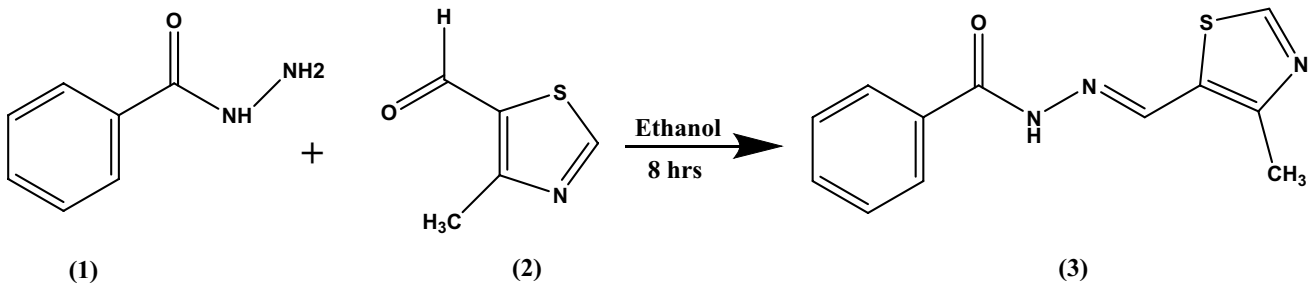

Scheme 1 Synthesis route of MMB compound

optoelectronic applications by fusing experimental research with DFT simulations.

2 Materials and methods

2.1 Experimental details

2.1.1 Material synthesis and crystal growth

All chemicals and solvents, including 4-methylthiazole-5-carboxaldehyde, benzohydrazide, and potassium hydroxide, were procured from Sigma Aldrich and used without further purification. The novel compound, (E)-N′-((4-methylthiazol-5-yl)methylene)benzohydrazide, was synthesized via a reflux method. A 1:1 molar ratio of 4-methylthiazole-5-carboxaldehyde (95 mg) and benzohydrazide (100 mg) was dissolved in ethanol under constant stirring in a round-bottom flask. Potassium hydroxide (41 mg) was added as a base catalyst, and the reaction was conducted under reflux for 8 h to promote complete condensation. After the reaction was completed, the mixture was allowed to cool to room temperature and filtered using Whatman filter paper to separate any solid impurities. The filtrate was then transferred to a beaker, covered with parafilm (pierced with small holes), and left to slowly evaporate at room temperature. After 15 days, the crystalline solids formed. These crude crystals were subjected to successive recrystallization from an ethanol solvent to further enhance purity. The recrystallization yielded well-defined pale yellow color, rectangular block-shaped crystals suitable for structural analysis. The synthesis route of MMB is depicted in Scheme 1, with corresponding ^{1}H and ^{13}C NMR spectroscopic data available in the supplementary section. A single-crystal, measuring 0.045 mm×0.085 mm×0.235 mm was selected for X-ray diffraction (XRD) analysis to determine the molecular structure of the synthesized compound. A photograph of the grown MMB single-crystal is shown in Fig. 1a.

2.1.2 Instrumentation

The MMB compound's NMR spectra (^{1}H and ^{13}C) were recorded in DMSO (Dimethyl sulfoxide) solvent utilizing an Agilent 600MR DD2 NMR spectrometer. The UV–vis absorption spectrum and solvatochromic spectra of different solvents were analyzed between 270 and 480 nm using a Beckman Coulter-DU-73 UV–visible spectrophotometer. The MMB compound PL was measured from 360 to 660 nm using the F-7000 FL spectrophotometer. Thermal properties of MMB were investigated via TGA/DTA on a NETZSCH STA 2500 system, with measurements taken under a nitrogen atmosphere from 30 to 500℃ at a heating rate of 10℃/min. The third-order nonlinear optical (NLO) properties, including the nonlinear refractive index, third-order susceptibility, and absorption coefficient, were assessed using the Z-scan method with the HOLMARC Z-scan model HOEDLOE-03.

2.1.3 X-ray data collection and structure refinement

The crystal structure of MMB ($C_{12}H_{12}N_3O_2S$) was determined using single-crystal X-ray diffraction (SCXRD) at ambient temperature. A suitable block-shaped crystal measuring 0.045 mm × 0.085 mm × 0.235 mm was carefully selected and mounted for analysis on a Bruker D8 Venture diffractometer equipped with a CuKα radiation source (λ = 1.54178 Å) and a large-area Photon III detector. SCXRD is a powerful technique for elucidating the three-dimensional arrangement of atoms in crystalline materials. When an incident X-ray beam interacts with the crystal, constructive

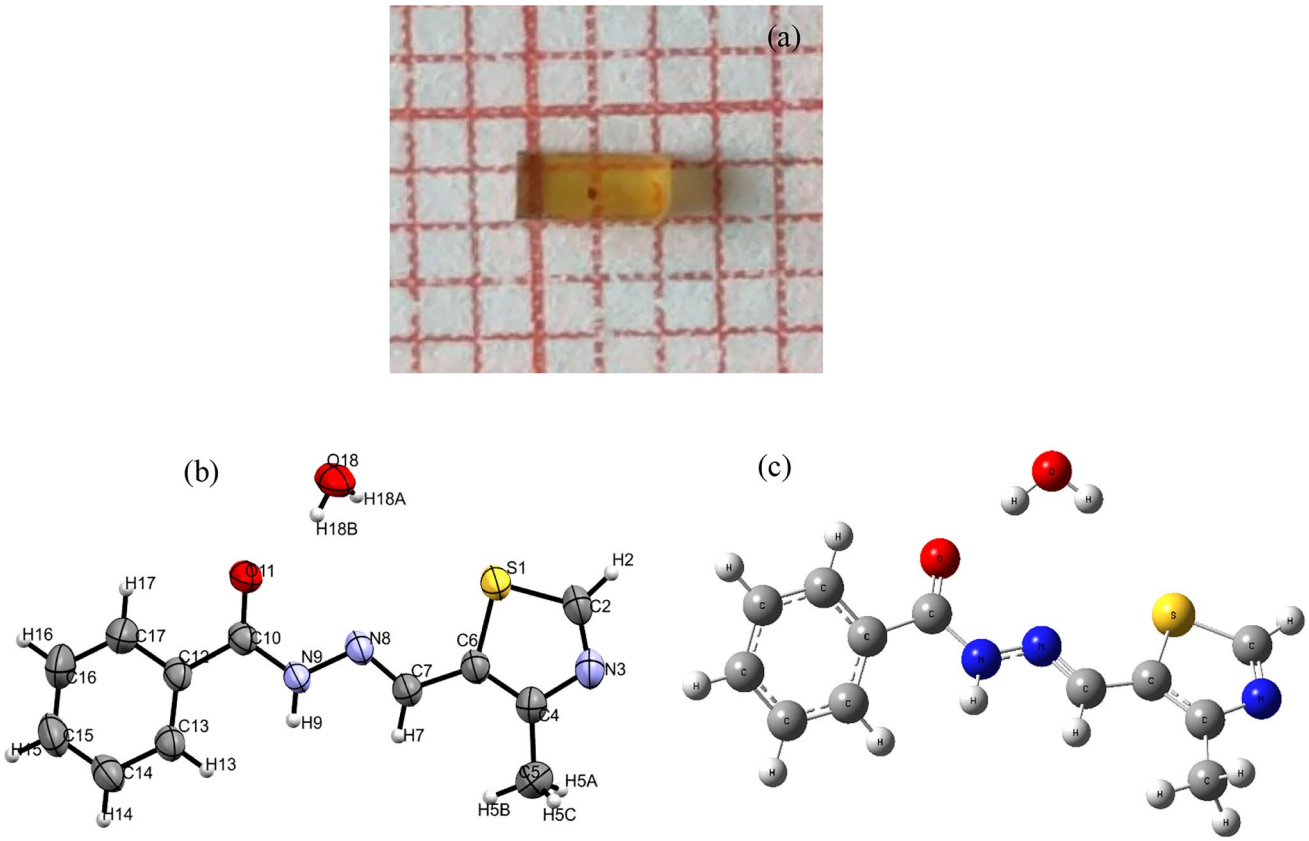

Fig. 1 (**a**)Photograph of the grown MMB single crystal, (**b**) ORTEP diagram, and (**c**) Optimized structure of MMB

interference occurs according to Bragg's law, producing a diffraction pattern. The intensities and positions of these diffracted beams are used to reconstruct the electron density within the unit cell, enabling precise determination of atomic positions, bond lengths, bond angles, and overall molecular geometry [21].

Data collection was carried out using a microfocus sealed-tube X-ray source to provide high-intensity illumination, and a multi-scan absorption correction (SADABS) was applied to account for variations in absorption, thereby enhancing data accuracy. The dataset was processed with Bruker SAINT software, yielding 2453 unique reflections for structure refinement. The structure was solved by direct methods and refined using full-matrix least-squares techniques in SHELXS-97 and SHELXL-2018 [22]. All non-hydrogen atoms were refined anisotropically, while hydrogen atoms were positioned geometrically and refined using a riding model. Refinement of 168 parameters against the 2453 reflections converged to final agreement factors of $R = 0.0350$ ($I > 2\sigma(I)$), $wR2 = 0.0859$ (all data), and a goodness-of-fit on F^2 of 1.024, indicating excellent agreement between observed and calculated diffraction data. Thermal ellipsoid plots were generated at the 50% probability level using Mercury 4.0 [23], and geometrical validation was performed using PLATON [24]. The crystallographic data have been deposited in the Cambridge Crystallographic Data Centre (CCDC-2260305) and are available at: http://www.ccdc.cam.ac.uk.

2.2 Computational details

The computational studies of the MMB compound, including geometry optimization, electronic absorption spectra, NBO analysis, HOMO–LUMO energy levels, and MEP analysis, were conducted using the Gaussian 09 software package [25]. Visualizations were performed with the GaussView 5 program. For all the above-mentioned analyses, the DFT method

was used in conjunction with the 6–311+ +G(d,p) basis set for carbon, oxygen, hydrogen, and nitrogen atoms. The electron density, ϱ(r), at bond critical points was calculated to gain insights into the bonding characteristics between atoms in the molecule, achieved through QTAIM analysis. The non-covalent interactions of the MMB molecule were investigated through RDG analysis using the *Multiwfn* 3.7 program [26], with visual representations generated using VMD software [27]. Additionally, the NLO properties, including the dipole moment, linear polarizabilities, and first and second hyperpolarizabilities were determined at different wavelengths (i.e., various frequencies) utilizing the TDHF approach with the 6–311++G(d,p) basis set in the GAMESS software [28].

3 Result and discussion

3.1 Crystal structure studies

The MMB crystal crystallizes in a monoclinic crystal system, as revealed by single-crystal X-ray diffraction analysis, and is categorized under the $P2_1/c$ space group, with four molecules present in each unit cell. The refined lattice parameters are: a = 4.8773(1) Å, b = 12.6252(3) Å, c = 21.2105(5) Å, $\alpha = 90°$, $\beta = 96.240(1)°$, and $\gamma = 90°$, offering key insights into the compound's structural configuration. Figure 1b presents the MMB's ORTEP diagram at a 50% probability level, while detailed crystallographic data and refinement information are provided in Table 1. Structurally, the MMB compound consists of a methyl-thiazole unit (S1-C2-N3-C4-C5-C6) and a phenyl moiety (C12-C13-C14-C15-C16-C17), connected by a methyleneformohydrazide group, which serves as a bridging unit. In the MMB structure, both the methyl-thiazole and phenyl rings exhibit planarity. The maximum deviation observed was 0.0044 Å for the C6 atom and 0.0039 Å for the C17 atom of both the methyl-thiazole and phenyl rings. The overall molecule adopts a non-planar conformation, with an 18.94° dihedral angle between the methylthiazole moiety and the phenyl ring. In the MMB compound, the methyleneformohydrazide group (O11=C10H10–N9H9–N8H8=C7H7) exhibits distinct bond characteristics based on the X-ray diffraction (XRD) analysis. The bond lengths for C12–C10, C10–N9, and N9–N8 were measured as 1.482 Å, 1.3457 Å, and 1.394 Å, respectively, confirming their singlebond nature. On the other hand, the C10 =O11 and N8=C7 bonds were found to have lengths of 1.235 Å and 1.274 Å, respectively, indicating double-bond character. The bond angles of N3–C4–C5 (119.9°) and C4–C6–S1 (118.2°) in the methyl-thiazole ring suggest a nearly planar trigonal geometry. The methyl group attached to the thiazole ring (N3–C4–C5) exhibits a slightly bent geometry, with a bond angle of 118.96°. Furthermore, in the MMB structure, the methyl group is positioned in a *anti* periplanar conformation relative to the methyl-thiazole ring, as evidenced by the torsion angle of 179.84° for C2–N3–C4–C5. Additionally, the torsion angle of C12–C13–C14–C15 (−0.09°) reveals that the ring adopts a *-syn* periplanar conformation.

The MMB compound's geometry was optimized using the B3LYP/6–311++G(d,p) method, as shown in Fig. 1c. The optimized bond lengths and angles generally conform to the experimental data, although minor deviations have been observed, particularly in the N–C, S–C, C–C, O–C, and N–N bonds (See Table S1). For example, in the phenyl rings C–C bond length is approximately 1.391 Å [29], and in our theoretical calculations, these bond lengths in the phenyl ring of MMB structure vary between 1.364 Å and 1.405 Å, which is consistent with experimental values (1.362 Å to 1.393 Å) and similar results have been observed in previously reported literature [29, 30]. The selected bond lengths, angles, and torsion angles for the MMB compound are listed in Table S1. Notably, the differences between experimental and theoretical bond lengths do not exceed 0.04 Å, and the deviations in bond angles are within 2°.

The MMB crystal structure was stabilized by a complex network of both intra and intermolecular hydrogen bonds, as illustrated in Fig. 2. The compound (E)-N'-((4-methylthiazol-5-yl)methylene) benzohydrazide forms these interactions through N–H…O, C-H…O, C-H…N and C-H… π contact. Notably, the nitrogen atom in the thiazole ring participates in hydrogen bonding with a CH group (C2–H2···N3), leading to a six-membered ring with the graph set motif $R_2^2(6)$ (See Fig. 3c). The inclusion of a water molecule facilitates the formation of additional $R_2^2(7)$ and $R_2^2(6)$ motifs involving the hydrazine bridge, further enhancing the stability of the crystal (as shown in Fig. 3c). Intramolecular interactions such as C17-H17…O11 (2.814 Å) and N9-H9…C13 (2.880 Å) also contribute significantly to the overall structural

Table 1 Crystal data and structure refinement details of MMB

Empirical formula	$C_{12}H_{13}N_3O_2S$
Formula weight	263.31
Temperature	293
Wavelength	1.54178 Å
Reflns. for cell determination	9848
θ range for the above	4.08° to 69.83°
Crystal system	Monoclinic
Space group	$P2_1/c$
Cell dimensions	$a = 4.8773(1)$ Å, $b = 12.6252(3)$ Å, $c = 21.2105(5)$ Å α = 90°, β = 96.240(1)° γ = 90°
Volume	1298.34 (5) Å^3
Z	4
Density(calculated)	1.347 Mg m^{-3}
Absorption coefficient	2.213 mm^{-1}
F_{000}	552
Crystal size	0.045 mm × 0.085 mm × 0.235 mm
θ range for data collection	4.08° to 70.20°
Index ranges	$-5 \le h \le 5$ $-15 \le k \le 15$ $-25 \le l \le 25$
Reflections collected	23,541
Independent reflections	2453
Absorption correction	Multi-scan
Refinement method	full-matrix least-squares on F^2
Data/restraints/parameters	2453/0/168
Goodness-of-fit on F^2	1.024
Final R indices [$I > 2\ \sigma(I)$]	*R1 = 0.0350, wR2 = 0.0859*
R indices (all data)	*R1 = 0.0454, wR2 = 0.0959*
Extinction coefficient	0.0011(3)
Largest diff. peak and hole	0.187; −0.159e Å^{-3}

stability. Detailed information regarding hydrogen bond interaction is given in Table 2. Furthermore, the MMB crystal packing is reinforced by face-to-face (Cg1–Cg2) interactions, where Cg1 denotes the centroids of the thiazole ring (S1–C2–N3–C4–C6) and Cg2 represents the centroids phenyl moiety (C12–C13–C14–C15–C16–C17). The distance between these centroids is 5.875 Å, (symmetry operation: -X, −1/2 + Y, 1/2-Z). Additionally, a C5-H5B… Cg2 interaction is observed at a distance of 5.447 Å, following the symmetry operation 1+X, Y, Z. The hydrogen bonding interaction and centroid interactions along the a-axis are depicted in Fig. 3a and b.

3.2 Optical studies

3.2.1 UV–Visible absorption studies

UV–Visible absorption spectroscopy is a crucial instrument for determining the E_g (Optical bandgap) and examining the photophysical characteristics of materials, particularly in the context of optoelectronic applications. The optical bandgap energy (E_g) signifies the energy required to elevate an electron from its initial state (ground state) to an excited state. To estimate E_g, Tauc's method [31] is often applied, which relates to the absorption coefficient (α) and the photon energy. This relationship is mathematically expressed as,

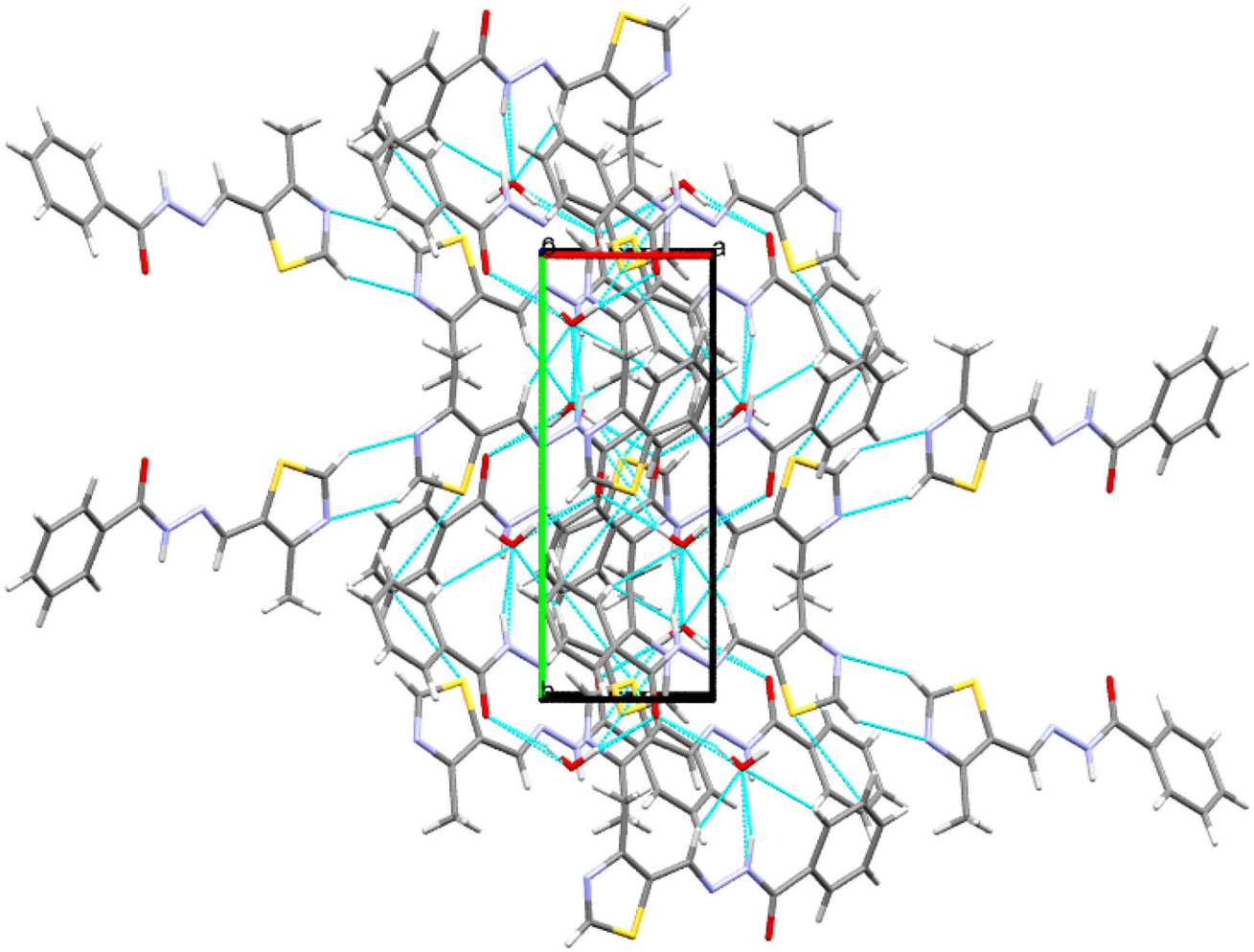

Fig. 2 Crystal packing of the MMB crystal is shown when viewed down c-axis

$\alpha h\upsilon = C\ (h\upsilon\text{-}E_g)^n$, where h, C, and υ are Planck's constant, proportionality constant, and photon frequency, respectively. The exponent n takes a value of 1/2 (direct transitions) and 2 (indirect transitions) [32, 33]. The transmission spectrum of MMB revealed that the studied sample exhibited a high transmittance (98.92%) across the visible region, with a cut-off of 331 nm (See Fig. 4a). According to this cut-off wavelength, the $\pi \rightarrow \pi^*$ excitation is associated with strong electronic transitions. This fusion of a well-defined cut-off and high transmittance suggests that the MMB crystal has minimal scattering losses, a low defect density, and superior crystalline quality. Such optical properties show that the material is ideal for applications involving optoelectronic and photonic devices.

The 'α' can be derived via the Beer-Lambert law, expressed as $\alpha = \frac{2.3026}{t}\ log\ \frac{1}{T}$, which is found to be 478.333 m^{-1}. To evaluate E_g, the plot of $(\alpha h\upsilon)^2$ versus photon energy ($h\upsilon$) is used, as shown in Fig. 4b. Extrapolated from the linear section of the curve until it intersects the x-axis at $\alpha = 0$ gives the value of E_g. Therefore, the E_g of the MMB was measured to be 3.48 eV. Beyond determining the bandgap energy, it is also possible to extract other linear optical properties from the absorption data, including extinction coefficient (K), reflectance (R), refractive index (n_o), complex dielectric constant (ε_c) and optical conductivity (σ_{op}) [34]. To characterize the linear optical properties of MMB, calculations were performed at the absorption peak wavelength (λ=324 nm), corresponding to the region where optical transitions occur. The extinction coefficient (K), which is directly related to the absorption coefficient and describes the attenuation of electromagnetic waves within the medium, was calculated using following relation:

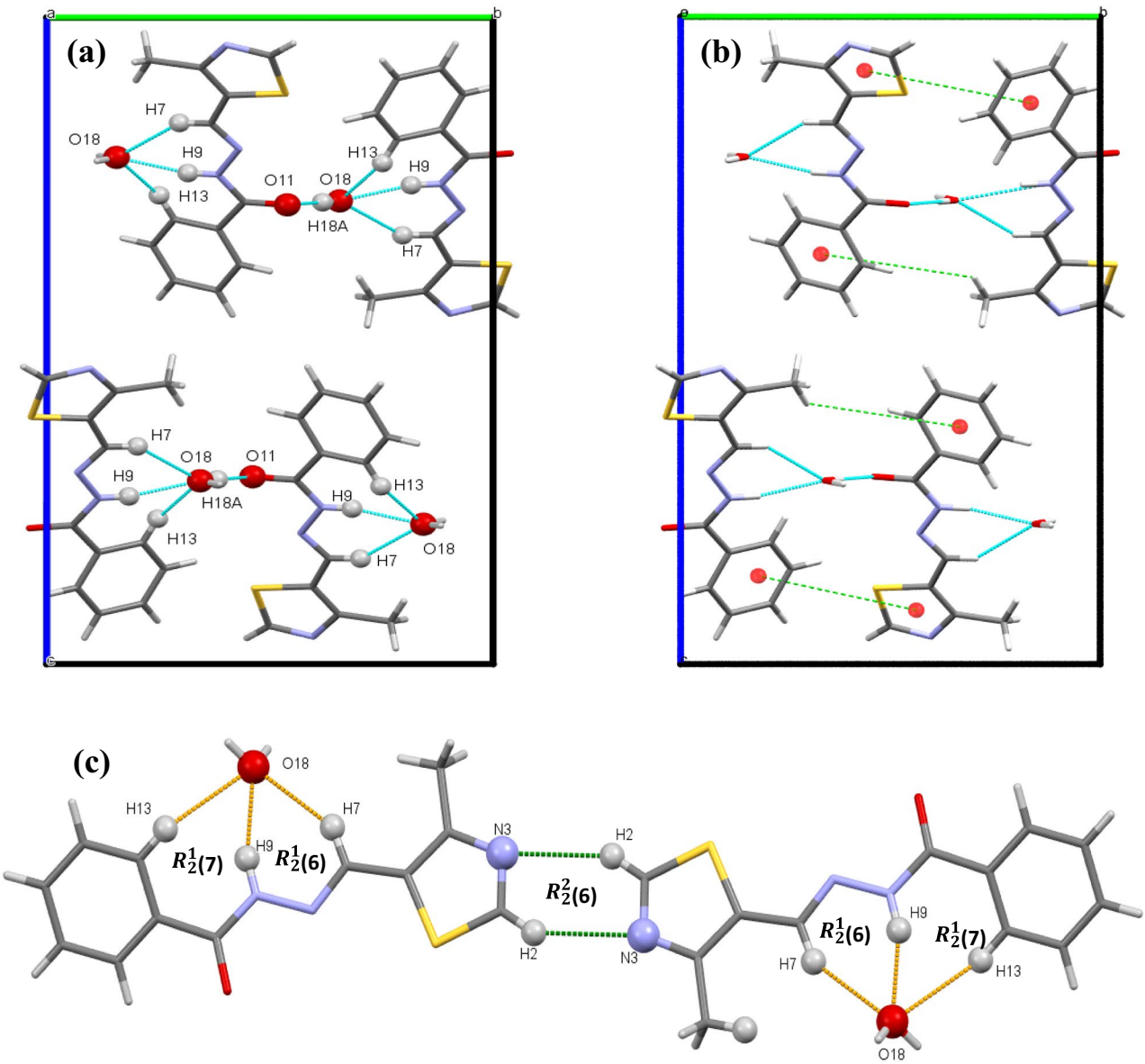

Fig. 3 Crystal packing interactions representation when viewed down a-axis: (**a**) C–H…O and N–H…O interactions (**b**) π…π and C-H… π interactions and (**c**) motif with $R_2^1(6)$ and $R_2^1(7)$ network

$$K = \frac{\alpha\lambda}{4\pi} \tag{1}$$

Here, λ=324 nm is absorption peak wavelength. At this wavelength, the extinction coefficient (K) was calculated to be 3.01×10^{-8}. This value is significantly lower than those typically reported for highly absorbing materials [35], indicating negligible optical absorption in the crystal. Such minimal absorption demonstrates the crystal's excellent optical transparency and confirms its potential for optoelectronic applications. The reflectance and refractive index were then determined using the following expressions [36];

$$R = \frac{\exp(-\alpha t) \pm \sqrt{\exp(-\alpha t)T - \exp(-3\alpha t)T + \exp(-2\alpha t)T^2}}{\exp(-\alpha t)T + \exp(-2\alpha t)T} \tag{2}$$

$$n_0 = \frac{-(1+R) \pm 2\sqrt{R}}{(1-R)} \tag{3}$$

Table 2 Intra and intermolecular hydrogen bonding geometry (Å, deg.) for the MMB crystal

D–H…A	D-H	H…A	D…A	D-H…A
C7-H7…O18[a]	0.930	2.394	3.214	146.87
N9-H9…O18[a]	0.860	2.095	2.922	161.13
C13-H13…O18[a]	0.930	2.618	3.425	145.54
C2-H2…N3[a]	0.930	2.605	3.435	149.02
C17-H17…O11[b]	0.93	2.526	2.814	98.20
N9-H9…C13[b]	0.860	2.546	2.880	104.21

[a]Intermolecular interaction

[b]Intramolecular interaction

Here, α and T are the absorption coefficient and transmittance respectively. Using reflectance data, the refractive index (n_0), calculated using Eq. (3), is plotted as a function of photon energy ($h\upsilon$) (see Fig. 4c). At a wavelength of 532 nm, the n_0 of MMB was measured to be 1.16, a key parameter for evaluating the third-order nonlinear optical susceptibility of the compound.

The complex dielectric constant (ε_c) of the MMB crystal was determined from n_0 and K. The complex dielectric constant (ε_c) is defined as $\varepsilon_c = \varepsilon_r + i\varepsilon_i$, where $\varepsilon_r = n_0^2 - K^2 is$ the real part of dielectric constant represents the material's ability to store electric energy, while $\varepsilon_i = 2n_0K$ is the imaginary part of dielectric constant corresponds to energy loss due to absorption. The calculated values were $\varepsilon_r = 1.345$ and $\varepsilon_i =$

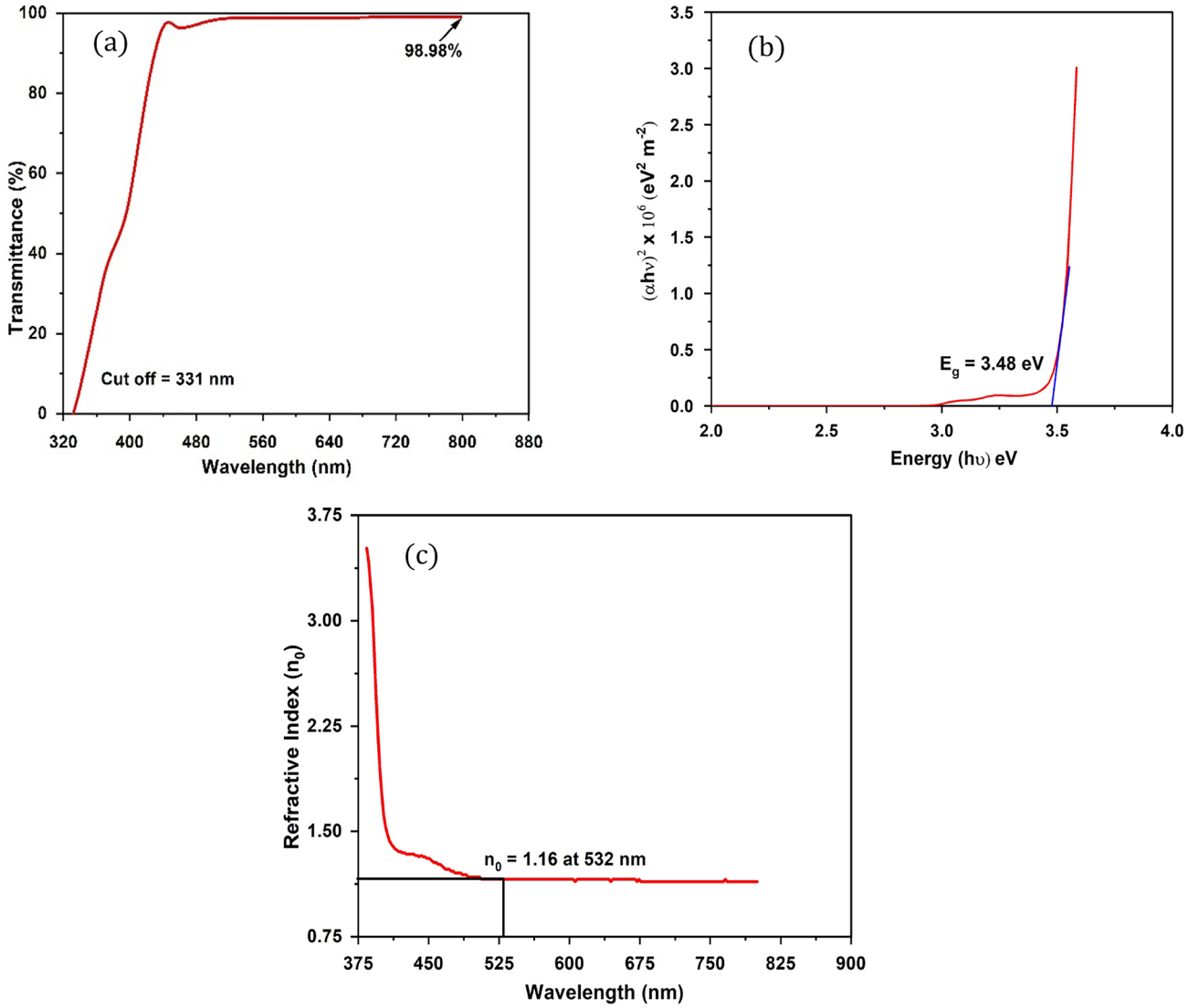

Fig. 4 (**a**) UV–Vis–NIR transmission spectrum, (**b**) Tauc's plot of the MMB, and (**c**) Variation of n_0 versus λ

6.96×10^{-8}. The overall dielectric constant (ε_c) was approximately 1.345, essentially equal to ε_r due to the negligible contribution of ε_i. The very small value of ε_i experiences negligible dielectric loss, which is favorable for optical applications requiring minimal attenuation.

Finally, the optical conductivity (σ_{op}), which describes the ability of the material to conduct optical energy under the influence of an electromagnetic field, was calculated using below expression [34]:

$$\sigma_{op} = \frac{\alpha n_0 c}{4\pi}, \tag{4}$$

where c is the velocity of light (3×10^8 m/s). The calculated σ_{op} was found to be 1.32×10^{10} S/m, which confirms that the MMB crystal can efficiently interact with light while maintaining low energy loss, which is essential for nonlinear optical and photonic device applications. Overall, the combination of high transparency, low absorption (α), negligible extinction coefficient (K), moderate refractive index (n_0), low dielectric loss, and optical conductivity (σ_{op}) demonstrates that the MMB crystal is an excellent candidate for advanced photonic and nonlinear optical applications, such as frequency conversion, optical modulation, and waveguiding.

3.2.2 *Photoluminescence (PL) studies*

Photoluminescence is a valuable technique for evaluating the optical and electronic properties of organic compounds. By measuring the emission of light subsequent to photon absorption, PL analysis provides crucial insights into electronic energy levels and emission processes, which are crucial for numerous optoelectronic applications [37]. We investigate the PL characteristics of the synthesized MMB compound, focusing on its emission spectrum and potential use in advanced photonic devices. The PL spectrum, obtained at room temperature with an excitation wavelength of 324 nm as determined by UV–Vis–NIR studies, exhibits a distinct emission peak at 448 nm (see Fig. 5a), indicating that the emitted light is situated within the blue spectral region of the electromagnetic spectrum. Notably, no further emissions peaks were observed, underscoring the high crystalline quality of the MMB crystal. The fluorescence bandgap energy was estimated for sharp intense spectra using the relation $E_g = hc/\lambda$, where λ is the emission wavelength, and h and c are universal constants. At 448 nm, the calculated fluorescence bandgap energy is found to be 2.76 eV. Moreover, the fluorescence characteristics were analyzed by utilizing the CIE chromaticity coordinate system, which provides a visual representation of the emission characteristics. The CIE diagram highlights the primary emission peak, indicating the dominant color of the emitted light. As shown in Fig. 5b, the coordinates (X = 0.16201, Y = 0.13688) fall within the blue region, marked by a circular symbol, demonstrating a noticeable color enhancement. These findings suggest that the MMB compound presents a promising prospect for blue light-emitting

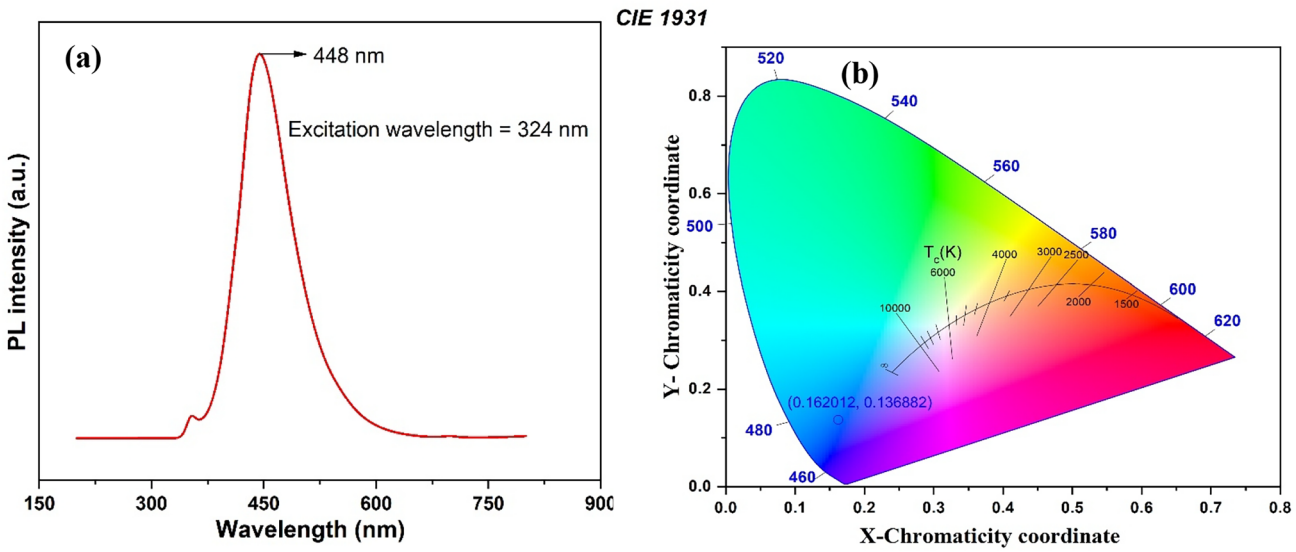

Fig. 5 (**a**) PL spectrum, (**b**) CIE chromaticity coordinates of an emission spectrum

materials, with potential applications in lighting and display technologies.

3.3 TG–DTA measurements

The thermal behaviour of the MMB compound was studied using TG and DTA in a dry nitrogen atmosphere, across a temperature range from 30 to 500℃, with a heating rate of 10℃ per minute. The corresponding TG–DTA curves are shown in Fig. 6. The thermogravimetric analysis, as depicted in Fig. 6, demonstrates that the MMB compound exhibits significant thermal stability, with no indications of decomposition or weight loss before 188.89℃. This indicates that there are no volatile substances or crystalline water present in the crystal lattice during growth. Two endothermic peaks appear in the DTA curve at 103.78℃ and 148.82℃ without any corresponding mass loss, suggesting that these events may be associated with solid–solid transitions, structural rearrangements, or minor relaxation phenomena rather than volatilization or decomposition. A major single-step weight loss of 95.4% is occurs between 188.9℃ and 363.8℃, leaving 2.5% residue around 454.5℃. The sharp endothermic peak at 313.85℃, occurring within this decomposition region, corresponds to the thermal decomposition temperature rather than the melting point of the compound, as it coincides with substantial weight loss [38]. The thermal stability of the MMB molecule is compared with that of other organic molecules containing hydrazide groups, as detailed in the literature [38–42], and is summarized in Table 3. Thus, the findings from TG–DTA studies suggest that the MMB material is suitable for nonlinear optical applications at temperatures up to 188.89℃.

Table 3 Comparison of thermal stability bevaviour of MMB with reported molecules

Compound	Thermal stability (℃)	References
MMB	188.89	Present work
4CP4MPE	160.23	[38]
BCA	153.28	[39]
4MPNP	186.90	[40]
THBSM	184.70	[41]
NEH	230.00	[42]

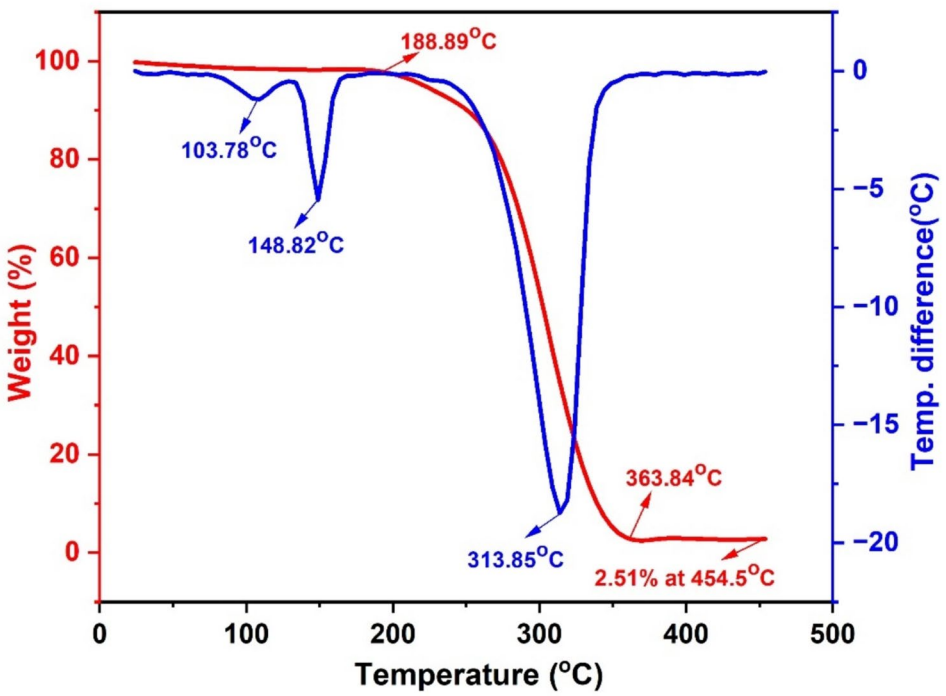

Fig. 6 TG–DTA curve of MMB compound

3.4 Solvatochromic studies

3.4.1 *Effects of solvents on MMB's fluorescence and absorption spectrta*

The solvatochromic behaviour of the MMB was investigated by analysing absorption and emission spectra across a variety of solvents with varying polarities. Solvatochromism describes the phenomenon in which the electronic absorption or emission spectrum of a compound changes in response to variations in solvent polarity, providing insights into the solute–solvent interactions [43]. In this study, the MMB compound displayed positive solvatochromism, showing bathochromic shifts in both absorption and emission spectra as solvent polarity increased. These shifts reflect the differential stabilization of MMB's ground and excited states by solvent molecules. In the absorption spectra, MMB revealed minor bathochromic shifts of 10 nm in the range of 324 to 334 nm from polar solvent ethanol to non-polar solvent chloroform, as depicted in Fig. 7a, indicating a slight stabilization of the ground state. This behavior, typical of $\pi \rightarrow \pi^*$ transitions, indicates that the ground state of MMB is relatively unaffected by solvent polarity, a characteristic observed in many organic chromophores where only weak solvent–solute interactions occur in the ground state [44]. Additionally, the molar extinction coefficient (ε) and oscillator strength (*f*) were calculated from the absorption spectra, varied with solvent polarity. Methanol solvent produced the highest extinction coefficient of 5.32×10^3 $Lmol^{-1}cm^{-1}$, while the oscillator strength peaked at 0.145 in acetonitrile, implying stronger light absorption and higher transition probabilities in more polar solvents. These findings suggest that polar solvents enhance solute–solvent interactions, particularly in the excited state, consistent with the observed solvatochromic shifts.

In the emission spectra, MMB also exhibited positive solvatochromism, exhibiting a bathochromic shift of 32 nm, from 420 nm in non-polar toluene to 452 nm in polar methanol (as depicted in Fig. 7b. These bathochromic shifts indicate that polar solvents provide greater stability to the excited state of MMB, which results in a reduction in the energy of emission. The augmentation of the Stokes shift, which is the difference between absorption and emission maxima, further supports this observation, indicating that solvent interactions are more efficacious in stabilizing the excited state as compared to the ground state. For example, the Stokes shift was 6586 cm^{-1} in toluene and 8530 cm^{-1} in ethanol. The FWHM of the emission peaks increased with increasing solvent polarity, with acetonitrile displaying the widest FWHM (68 nm) suggesting enhanced vibrational relaxation in the excited state in polar environments. The observed solvatochromic shifts in MMB can be attributed to stronger dipole–dipole interactions between the solute and solvent, especially in polar solvents. These interactions preferentially stabilize the excited state.

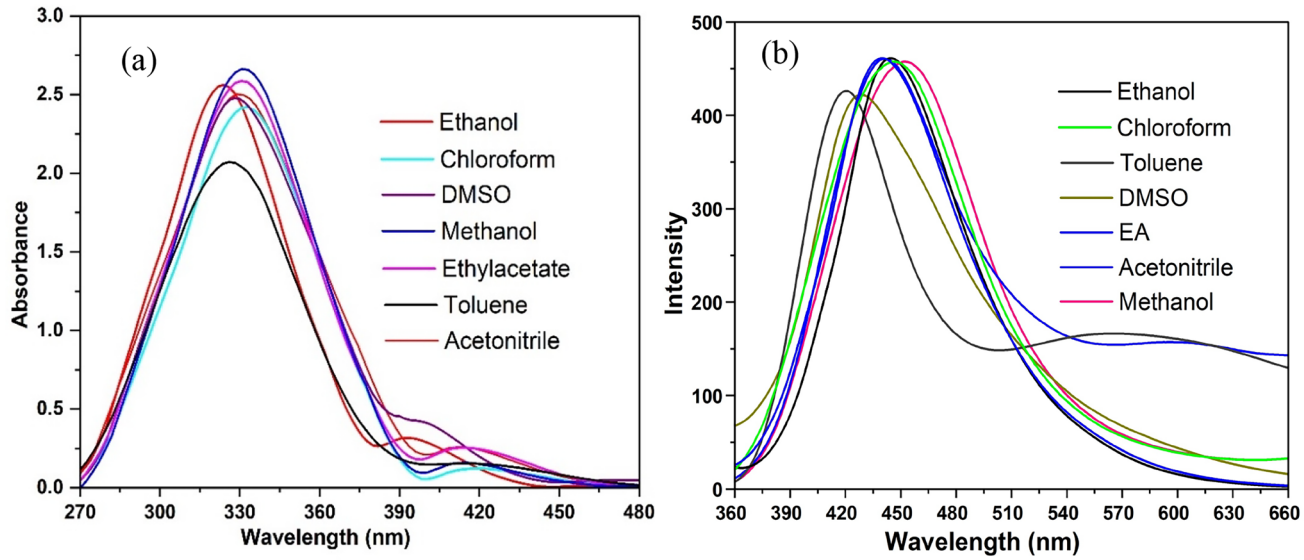

Fig. 7 (**a**) Absorption and (**b**) Emission spectra in different solvents for MMB

Specific interactions, such as hydrogen bonding, may also play a significant role in certain solvents, such as ethyl acetate, where the shift was less pronounced. Similar studies on organic chromophores show that solvent polarity significantly affects photophysical behavior. In general, the solvatochromic analysis of the MMB compound exhibits solvent-dependent bathochromic shifts in both absorption and emission spectra, with polar solvents more effectively stabilizing the excited state. These findings emphasize the important role of solvent choice in tuning the optical properties of MMB, making it a promising candidate for applications in optoelectronics and molecular sensing [45].

3.4.2 *Calculation of NLO parameters (α_{CT}, β_{CT} and γ_{CT}) from solvatochromic data*

The solvatochromic method was employed to investigate the NLO characteristics of the MMB, revealing significant variations influenced by solvent polarity. The linear polarizability (α_{CT}) exhibited the lowest value (2.66×10^{-24} e.s.u.) in toluene and the highest value (3.40×10^{-24} e.s.u.) in acetonitrile. This variation exemplifies the enhanced capability of more polar solvents to stabilize the MMB structure, resulting in enhanced polarizability. First hyperpolarizability (β_{CT}) values were calculated, with the lowest at 1.72×10^{-28} e.s.u. in toluene and the highest at 2.21×10^{-28} e.s.u. in acetonitrile. The results suggest that the dielectric environment of the solvent is important for facilitating charge transfer transitions, which are essential for potential applications in nonlinear optics [46]. Additionally, the second hyperpolarizability (γ_{CT}) was determined, revealing the lowest values at 0.99×10^{-32} e.s.u. in toluene and the highest values at 1.28×10^{-32} e.s.u. in acetonitrile. The observed increase in γ_{CT} with solvent polarity signifies that the solvent environment significantly impacts electron polarization processes within the MMB, enhancing its suitability for NLO applications [47]. The formulas used for calculating linear polarizability, first hyperpolarizability, and second hyperpolarizability are described in my previous article [11], while the calculated NLO parameters and experimental photophysical parameters are summarized in Tables 4 and 5.

Table 5 Transition dipole moment (μ_{eg}), polarizabilities (α_{CT}), first and second hyperpolarizabilities (β_{CT} and γ_{CT}) of the MMB

Solvents	$\mu_{eg}^2 \times 10^{-36}$e.s.u	$\alpha_{CT}\times 10^{-24}$e.s.u	$\beta_{CT} \times 10^{-28}$e.s.u	$\gamma_{CT} \times 10^{-32}$e.s.u
Ethanol	8.70	2.83	1.81	1.02
Chloroform	8.89	2.99	1.96	1.14
Toluene	8.05	2.66	1.72	0.99
Acetonitrile	10.22	3.40	2.21	1.28
Methanol	9.85	3.30	2.16	1.26
Ethyl acetate	9.54	3.18	2.08	1.21
DMSO	9.55	3.17	2.06	1.18

Table 4 Photophysical Properties of MMB

Solvents	λ^a_{abs}(nm)	λ^b_{abs}(cm^{-1})	λ^c_{emi}(nm)	λ^d_{emi}(cm^{-1})	FWHM (nm)	$\varepsilon^e \times 10^3$ $Lmol^{-1}$ cm^{-1}	f^g_{abs}
Ethanol	324	30,864	448	22,321	56	5.10	0.126
Chloroform	334	29,940	450	22,222	62	4.82	0.125
Toluene	329	30,395	420	23,809	63	4.16	0.115
Acetonitrile	331	30,211	442	22,624	68	5.00	0.145
Methanol	333	30,030	452	22,123	62	5.32	0.139
Ethyl acetate	332	30,120	442	22,624	61	5.20	0.135
DMSO	330	30,303	428	23,364	64	4.96	0.136

[a]Absorption maxima in nm

[b]Absorption maxima in cm^{-1}

[c]Emission maxima in nm

[d]Absorption maxima in cm^{-1}

[e]Molar extinction coefficient at absorption maxima

[g]Oscillator strength

3.5 Hirshfeld surface (HS) analysis

HS analysis provides an insightful visualization of molecular interactions within a crystal by mapping distances between atoms using the d_i (internal) and d_e (external) parameters. This analysis highlights regions with different interaction strengths: red regions indicate strong interactions, white neutral, and blue weak forces. Understanding these interactions is crucial for applications in nonlinear optics (NLO), where the molecular arrangement directly influences optical behaviors such as the third harmonic generation (THG) [48]. A key component of HS analysis is the fingerprint plot—a 2D representation derived from the surface that concisely displays intermolecular interactions by quantifying atomic proximities and interaction types. This plot can reveal critical forces such as hydrogen bonding and π-π stacking or other pivotal molecular interactions [49].

In this study, HS analysis for the MMB compound was conducted using *Crystal Explorer 17* [50]. The results indicate that the d_{norm} parameter, which reflects normalized contact distances incorporating d_i, d_e, and van der Waals radii, ranged from −0.5719 Å to 1.4582 Å. The Hirshfeld surface analysis reveals deep red spots on the surface, indicating strong interactions, mainly associated with oxygen and nitrogen atoms. This confirms their role in weak hydrogen bonding (see Fig. 8a). This interpretation is supported by the significant spike observed in the corresponding fingerprint plot. The low curvature regions on the HS indicate the existence of close contacts, which may indicate potential covalent bonding interactions. Additionally, broad, flat blue regions on the surface imply the presence of π-π stacking interactions between molecules (See Fig. 8b). The shape index provides further insight: red triangular regions denote concave areas, indicating where atoms from neighboring stacked molecules are interacting with the surface, while blue triangular regions (convex areas) correspond to the surface atoms of the molecule, such as those in aromatic rings (See Fig. 8c). Furthermore, the prominent circular

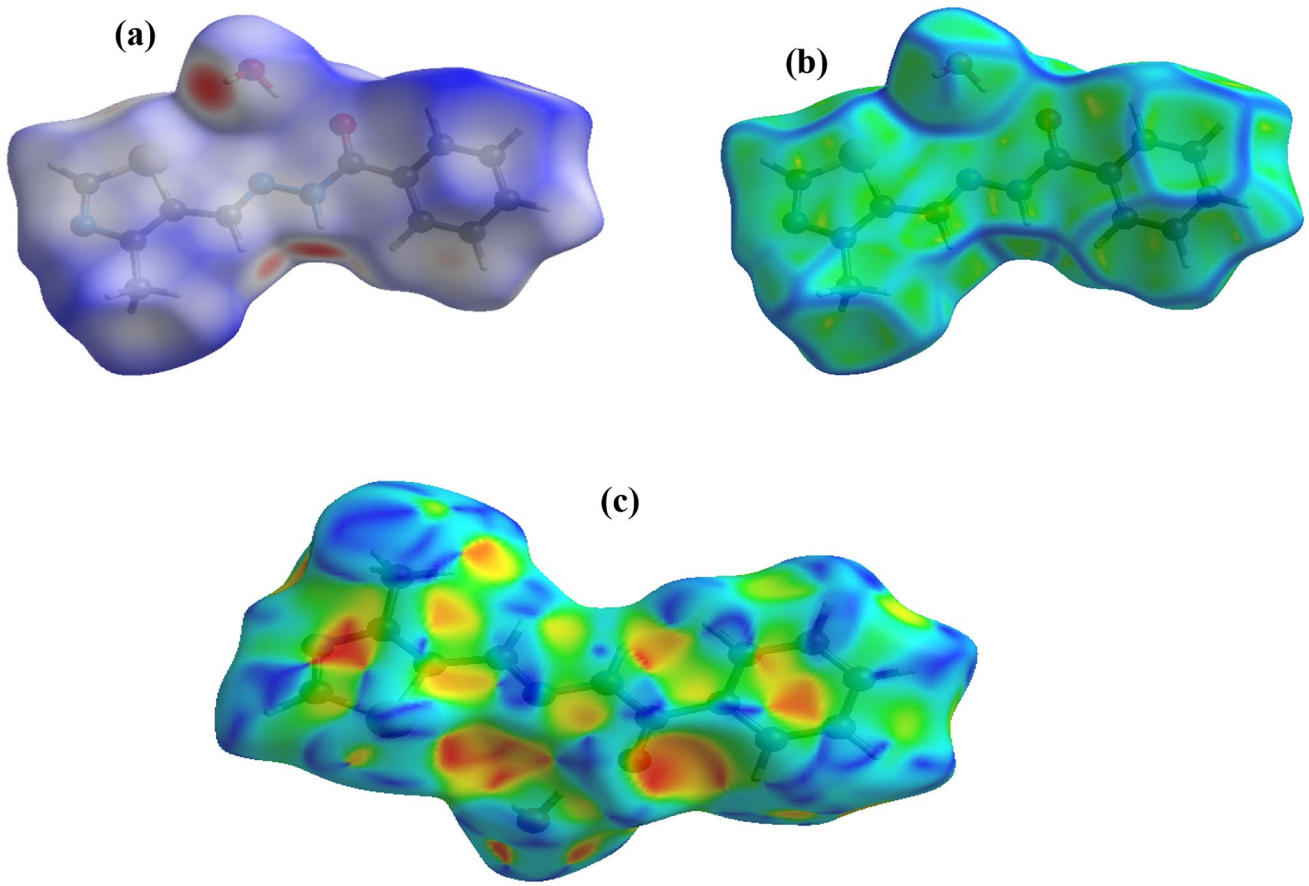

Fig. 8 Hirshfeld surfaces of the MMB crystal mapped with; (**a**)d_{norm} (**b**)Curvedness and (**c**) Shape index

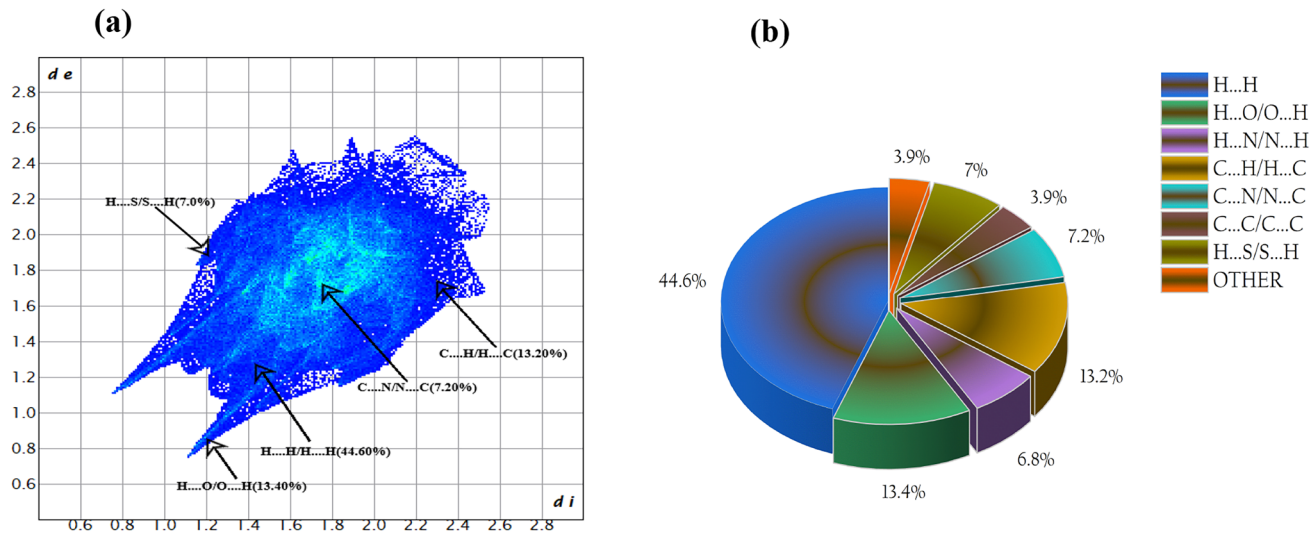

Fig. 9 Fingerprint plots of the MMB showing (**a**) All interactions, (**b**) 2D fingerprint plot represented in a pie chart

depressions (deep red) observed at the edges of the Hirshfeld surfaces are attributed to significant hydrogen bonding interactions. Conversely, red points on the surface indicate short contacts, including C–H…N, and C–H…O, interactions, which play a critical role in stabilizing the crystal structure [51].

The fingerprint plot reveals that hydrogen–hydrogen (H–H) interactions are the most dominant, accounting for 44.6% of the total intermolecular contacts (See Fig. 9a). This is typical in organic compounds, where such interactions play a key role in stabilizing the molecular framework. Other significant interactions comprise hydrogen–oxygen (H–O) at 13.4% and carbon-hydrogen (C-H) at 13.2%, indicating weak hydrogen (H) bonding and van der Waals forces that aid in maintaining the structural integrity. Interactions involving sulfur and nitrogen are also present, with H–S contributing 7% and H-N 6.8%. Additionally, C–N and C–C interactions account for 7.2% and 3.9%, respectively, highlighting the role of covalent bonding and π-π stacking. The fingerprint plots of the MMB compound, showing all interactions and a 2D fingerprint plot represented in a pie chart, are displayed in Figs. 9a and b. Together, these intermolecular forces, such as hydrogen bonding, van der Waals interactions, and stacking, govern the packing and stability of the MMB crystal. The significance of this structural stability lies in its NLO characteristics, as the arrangement of molecules directly influences the material's response to external optical stimuli [49].

3.6 Natural bond orbital (NBO) analysis

The NBO analysis is an important computational technique used to examine the electronic structure of molecules, focusing on electron delocalization and intramolecular interactions. This study elucidates key factors such as bonding characteristics, charge transfer, and resonance stabilization, which are essential for assessing molecular stability and reactivity [52]. The comprehension of these electronic characteristics holds significant significance in evaluating potential applications in nonlinear optics. The NBO analysis for the studied compound was conducted at the B3LYP/6–311++G(d,p) level using Gaussian software, with significant results tabulated in Table 6.

The results in Table 6 demonstrate that ICT (intramolecular charge transfer) interactions, particularly between π and π* orbitals, are critical for stabilizing the molecule. The strongest interactions occur between lone pairs (LP) and π* orbitals, as well as π to π* transitions. Notably, the interaction between the lone pair (LP) on N8 and the π* orbital of C7–O16 results in a maximum stabilization energy ($E^{(2)}$) of 46.14 kJ/mol, highlighting the effective electron-donating ability of the nitrogen lone pair. This delocalization of electrons into the π* orbital enhances the overall stability by increasing the electron density in the π* orbital, thereby lowering the system's energy. Additionally other significant π to π* interactions were observed, such as; π(C1–C3) → [π*(C2–C6),

Table 6 Selected Lewis and non-Lewis interactions from Second order perturbation theory analysis of Fock matrix for MMB molecule

Donar NBO (i)	E_D (i)(e)	Acceptor NBO (j)	E_D (j)(e)	$E^{(2)}$ kJ/mol	ΔE^a a.u	$F(i,j)^b$ a.u
π (C1-C3)	1.6426	π* (C2-C6)	0.321	21.21	0.28	0.069
		π* (C4-C5)	0.37	20.17	0.27	0.066
π (C2-C6)	1.6470	π* (C1-C3)	0.2912	18.07	0.29	0.065
		π* (C4-C5)	0.379	21.45	0.27	0.069
π (C4-C5)	1.6590	π* (C1-C3)	0.293	18.92	0.29	0.067
		π* (C2-C6)	0.321	18.66	0.28	0.065
		π* (C7-O16)	0.291	17.38	0.29	0.064
π (N9-C10)	1.9273	π* (C11-C12)	0.334	9.20	0.36	0.055
π (C14-N15)	1.8730	π* (C11-C12)	0.334	19.30	0.34	0.076
σ (C11-S13)	1.9732	σ* (C12-C24)	0.021	5.66	1.07	0.069
σ (S13-C14)	1.9849	σ* (C10-C11)	0.026	7.10	1.15	0.062
LP (1) N8	1.6637	π* (C7-O16)	0.291	46.14	0.31	0.109
		π* (N9-C10)	0.216	27.62	0.28	0.081
LP (1) N9	1.9180	σ* (N8-H28)	0.037	8.55	0.79	0.074
		σ* (C10-H22)	0.035	10.54	0.81	0.083
LP (2) S13	1.6206	π* (C11-C12)	0.334	18.83	0.27	0.064
		π* (C14-N15)	0.325	29.77	0.24	0.077
LP (1) N15	1.8994	σ* (C11-C12)	0.034	6.69	0.94	0.072
		σ* (S13-C14)	0.062	14.20	0.57	0.081
LP (2) O16	1.8624	σ* (C4-C7)	0.063	19.61	0.68	0.105
		σ* (C7-N8)	0.080	26.86	0.68	0.123

[a]Energy difference between donor orbital (i) and acceptor (j) orbital ΔE = E(i)-E(j) a.u

[b]F(i,j) is the Fock matrix element between i and j NBO orbitals in the a.u unit

π*(C4–C5)], π(C2–C6) → [π*(C1–C3), π*(C4–C5)], and π(C4–C5) → [π*(C1–C3), π*(C2–C6), π*(C7–O16)]. The corresponding $E^{(2)}$ values for these interactions are 21.21, 20.17, 18.07, 21.45, 18.92, 18.66, and 17.38 kJ/mol, respectively. These π to π* transitions promote electron delocalization across conjugated systems, reinforcing resonance stability within the molecular framework. This delocalization allows for a redistribution of charge density, minimizing localized repulsion and stabilizing the entire structure. Moreover, lone pair interactions significantly contribute to the molecule's stability through hyperconjugative effects involving nitrogen and sulfur atoms. Noteworthy interactions include LP (1) N9 → σ* (C10–H22), with an $E^{(2)}$ of 10.54 kJ/mol and LP (2) S13→[π*(C14–N15), π*(C11–C12) with an $E^{(2)}$ of 29.77 and 18.83 kJ/mol respectively. These interactions serve to stabilize the molecular structure by reducing electron repulsion and enhancing delocalization into nearby antibonding orbitals, thereby effectively lowering the energy barrier for rotation around the bonds and enhancing molecular flexibility. In conclusion, the NBO analysis reveals that extensive hyperconjugation and ICT interactions significantly stabilize the electronic structure of the MMB. The substantial charge transfer across π and lone pair orbitals underscores the importance of these interactions in enhancing stability and suggests the molecule's potential in nonlinear optical (NLO) applications due to its favourable charge transfer characteristics [53].

3.7 Frontier molecular orbital (FMO) and molecular electrostatic potential (MESP) plot analysis

Frontier Molecular Orbital (FMO) study evaluates the molecule's kinetic stability and chemical

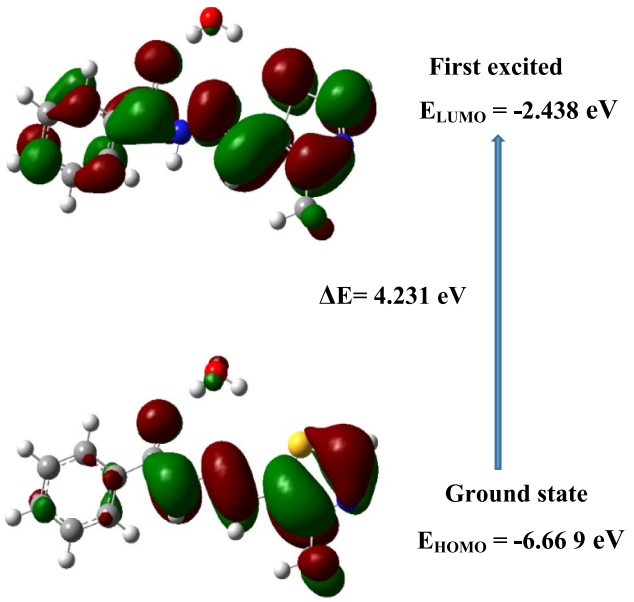

Fig. 10 Frontier molecular orbitals plot for MMB

reactivity using DFT and an appropriate basis set [54]. In FMO theory, the HOMO represents the molecule's electron-donating capacity, whereas the LUMO represents its electron-accepting capacity [55]. The HOMO–LUMO energy gap gives important information about the molecule's reactivity and stability [56]. Accordingly, the FMO analysis of MMB reveals key insights into its electronic properties and reactivity. It can be observed from Fig. 10 that the HOMO energy of −6.669 eV indicates that the molecule is stable and predominantly localized in the thiozole moiety, requiring significant energy to donate electrons. Conversely, the LUMO is delocalized in the complete molecule, with an energy of −2.438 eV indicating its potential to accept electrons, indicating moderate electrophilic behavior. The HOMO–LUMO gap of 4.231 eV suggests that MMB is chemically stable, but reactive enough to engage in electron transfer processes. The ionization potential of 6.669 eV confirms that MMB resists the loss of electrons, while the electron affinity of 2.438 eV highlights its moderate ability to gain electrons. The global hardness of the molecule, calculated as 2.115 eV, further underscores its stability, while its softness value of 0.236 eV indicates a relatively low level of reactivity. The chemical potential of −4.553 eV suggests a stable electronic environment, and the electronegativity of 4.533 eV indicates a balanced electron-attracting ability. The energies of the FMO, along with their global chemical reactivity descriptor values, for the MMB molecule are presented in Table 7. The localization of the HOMO on the thiazole donor unit and the delocalization of the LUMO across the entire π-conjugated framework confirm an efficient intramolecular charge transfer (ICT) pathway within MMB. Such ICT processes, facilitated by the moderate HOMO–LUMO energy gap, enhance the molecule's polarizability and nonlinear optical susceptibility ($\chi^{(3)}$), thereby directly contributing to the observed third-order NLO response under CW excitation at 532 nm.

The three-dimensional Molecular Electrostatic Potential (MESP) graphic depicts the electronic structure of a molecule by displaying the distribution of electron density and polarization. This method is very beneficial for detecting nucleophilic and electrophilic sites in the molecule. Figure 11 depicts the MESP values for compound MMB with a color gradient having a potential value transitioning from negative to positive, represented by a change

Table 7 FMO's energies with global chemical reactivity descriptor (GCRD) properties

GCRD parameters	Symbol and formulae	Values
E_{HOMO}	E_H (eV)	− 6.669
E_{LUMO}	E_L (eV)	− 2.438
$\Delta E_{LUMO\text{-}HOMO}$	$E_g = E_{L\text{-}H}$ (eV)	4.231
Ionization potential (I)	$I = -E_{HOMO}$ (eV)	6.669
Electron affinity (A)	$A = -E_{LUMO}$ (eV)	2.438
Global Hardness (η)	$\eta = (E_{LUMO} - E_{HOMO})/2$ (eV)	2.115
Softness (S)	$S = 1/2\eta$ $(eV)^{-1}$	0.236
Chemical potential (μ)	$\mu = (E_{LUMO} + E_{HOMO})/2$ (eV)	− 4.553
Electronegativity (χ)	$\chi = -\mu$ (eV)	4.533
Electrophilicity (ψ)	$\psi = \mu^2/2\eta$ (eV)	4.893

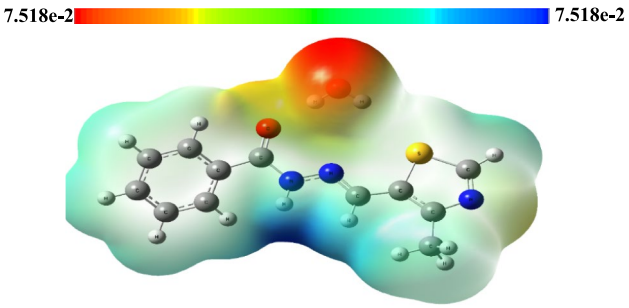

Fig. 11 Molecular Electrostatic potential plot (MESP) plot for MMB

from deep red to deep blue. In this graphic, the blue patches exhibit positive potential values, signifying electron-deficient (or positively charged) areas with decreased electron density. On the other hand, red patches indicate negative potential values, indicating electron-rich (negatively charged) zones with increased electron density [57, 58]. Figure 11 illustrates that a deep red region is present around the oxygen atom of the water molecule, which is crucial for serving as a nucleophile attacker. Conversely, the lighter blue patches surrounding hydrogen atoms indicate electron-deficient regions, which are prone to electrophilic interactions. The oxygen atom present in the molecule serves as a reactive site probe for both intra and intermolecular interactions.

3.8 Quantum theory of atoms in molecule (QTAIM) and noncovalent interactions (NCI)

The QTAIM is a valuable approach for understanding weak interactions such as halide and hydrogen (H) bonding, C-H**…**π interactions, aromatic ring stacking (π-π stacking), as well as electrostatic and dispersion forces. It is a powerful tool for understanding the non-covalent interactions that influence the electronic structure and stability of molecules. This is crucial for determining their nonlinear optical properties. By examining bond critical points (BCPs) and the distribution of electron density, QTAIM reveals the nature of weak interactions including, hydrogen (H) bonding, C-H**…**π interactions, and π-π stacking. These interactions play a significant role in enhancing charge delocalization, polarizability, and ICT pathways, which are all key factors in the NLO response. For instance, π-π stacking can extend conjugation across aromatic systems, increasing dipole moments and hyperpolarizability-essential features for materials exhibiting strong NLO behaviour. Furthermore, non-covalent interactions stabilize specific conformations that optimize charge transfer, enhancing NLO properties. Hence, understanding and designing molecules with enhanced NLO effects requires a comprehensive understanding of electronic density and molecular topology [26, 59].

The topological parameters of the molecule are depicted in Table 8. Consequently, the molecule is characterized by three distinct interactions, namely C7-O16…H31, C11-S13…H30, and C10-H22…H25 with their respective bond critical points (as depicted in Fig. 12). All three interactions have bond critical points with a (3, −1) topology, which indicates a bond path connecting the atoms and a minimum electron density along the bond path. The C11-S13…H30 interaction has the highest electron density (0.0359 a.u.), indicating a stronger interaction compared to the others. While C7-O16…H31 has a moderate electron density (0.0234 a.u.), while C10-H22…H25 shows the weakest interaction (0.00846 a.u.). The ratio -G(r)/V(r) helps to identify the nature of the bond. For C7-O16…H31, the ratio is close to 1 (1.005), suggesting a weak covalent nature. The C11-S13…H30 interaction has a ratio of 1.687, and C10-H22…H25 has 1.474, both indicating non-covalent interactions (likely van der

Table 8 QTAIM-derived topological analysis with respective bond critical points for the MMB compound

Interactions	C7-O16…H31	C11-S13…H30	C10-H22…H25
Bond Critical Point BCP	65	66	36
Bond Critical Point type	(3, − 1)	(3, − 1)	(3, − 1)
Electron Density ρ_{BCP}(a.u.)	0.0234	0.0359	0.00846
Lagrangian Kinetic Energy G(r) (a.u.):	0.0176	0.00238	0.00643
Potential Energy Density V(r) (a.u.):	− 0.0175	− 0.00141	0.00436
$^{-}$G(r)/V(r):	1.005	1.687	1.474
$\lvert\lambda_1\rvert/\lambda_3$	0.226	0.143	0.174
Energy Density E(r)	0.000135	0.000965	0.00206
Laplacian of Electron Density $\nabla^2\rho$(a.u.)	0.0711	0.0101	0.0339
Total ESP (a.u.)	0.112	− 0.0498	0.0936
Eigenvalues of Hessian matrix ($\lambda_3>0,\lambda_2<0,\lambda_1<0$)	0.13144, − 0.0304, − 0.0298	0.0188, − 0.00275, − 0.00269	0.0463, − 0.00425, − 0.00810

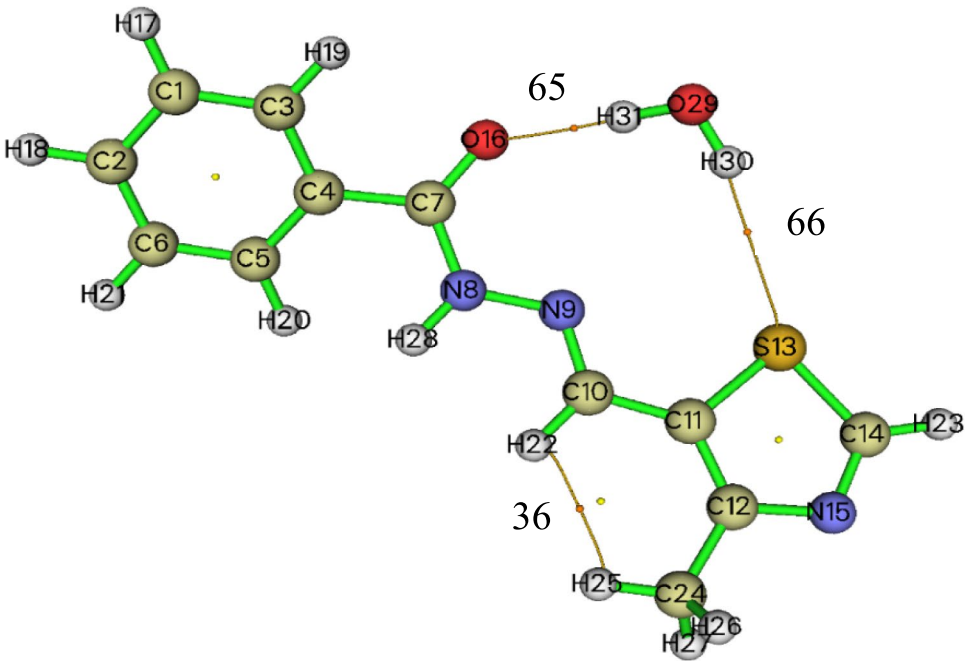

Fig. 12 Bond Critical Point for the MMB compound

Waals or hydrogen bonding). The eigenvalues for all three interactions are less than 1, confirming they are non-covalent. Covalent bonds usually have values greater than 1. The C7-O16…H31 interaction exhibits a positive ESP (0.112 a.u.), indicating a region of electron-rich density, while C11-S13…H30 exhibits a negative ESP (−0.0498 a.u.), indicating a more attractive electrostatic interaction. The interaction C11-S13…H30 is the strongest non-covalent interaction based on electron density and energy parameters. The C7-O16…H31 interaction is moderately strong and has covalent-like characteristics, while C10-H22…H25 is the weakest, with a distorted electron density. All interactions are non-covalent, with different contributions to the overall stability of the molecule.

Non-covalent interactions (NCIs) are crucial in highlighting the NLO properties of compounds [60]. The Reduced Density Gradient (RDG) analysis serves as a topological tool to reveal NCIs, including hydrogen (H) bonds, van der Waals interactions and, steric effects. RDG is mathematically expressed as:

$$R(r) = \frac{1}{2\left(3\pi^2\right)^{\frac{1}{3}}} \frac{|\nabla\rho(r)|}{\rho(r)^{\frac{4}{3}}}, \tag{5}$$

where $R(r)$ is a function of the electron density $\rho(r)$ and its gradient, representing the density's inhomogeneity at any given point in space r. Reduced Density Gradient (RDG) scatter plot, typically used to identify and visualize non-covalent interactions (NCIs) in molecular systems. The RDG isosurface was examined using the *Multiwfn* software [26], while VMD software [27] was employed for visualization. The RDG plot is generated by graphing R(r) versus ($sign(\lambda 2)\ \rho(r)$). Accordingly, the molecular structure with RDG isosurfaces (See Fig. 13) is visualized using colour coding to highlight different types of non-covalent interactions. The green isosurfaces represent weak interactions, such as van der Waals forces, between atoms that are not forming strong bonds but still influencing each other. The red isosurface formation within the aromatic rings indicates regions of steric repulsion. Lastly, the bluish-green to red regions suggest a mixed region, where both weak interactions (van der Waals) and repulsive forces (steric effects) are present. This is due to the existence of functional groups, where space is limited, but weak bonds still form. Similarly, the multiple spikes and regions in a scattered plot (Fig. 13) show a clear division of interactions. The negative spikes signify strong attractive interactions, and the positive spikes indicate steric repulsions.

3.9 Nonlinear optical studies

3.9.1 Third-order nonlinear optical studies

In this study, we examined the nonlinear optical response of the MMB compound using the Z-scan

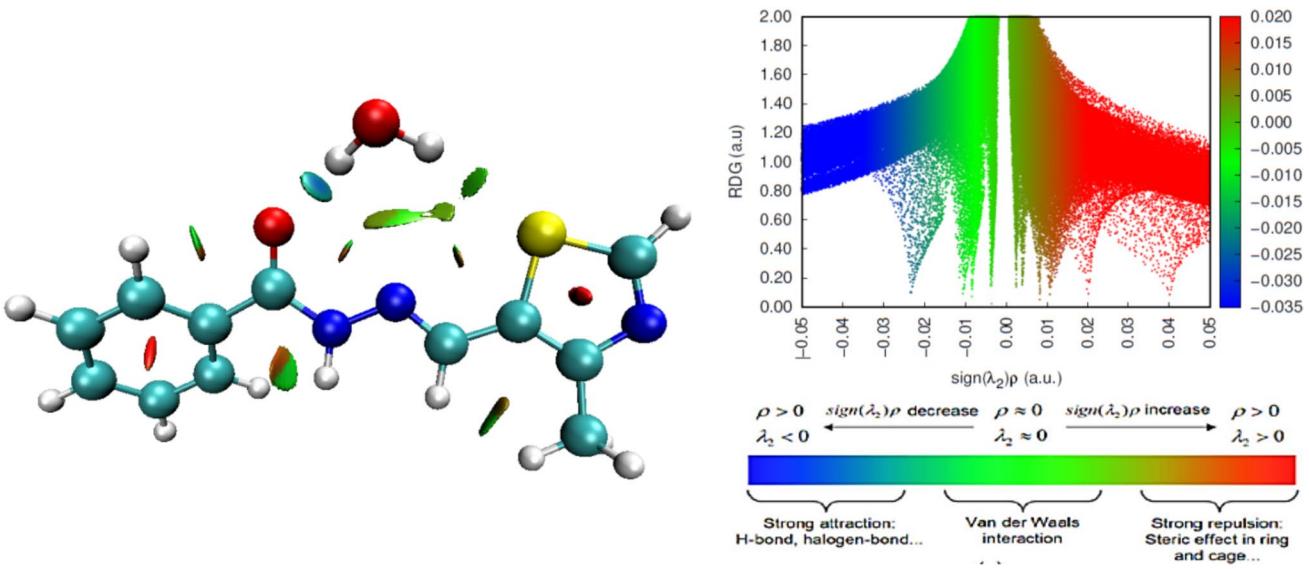

Fig. 13 Non-covalent interactions isosurfaces of electron density and, 2D scattered map of RDG vs sign(λ2)ρ(r)

technique, which is a powerful and sensitive tool for investigating nonlinear absorption and refraction in materials. The method involves translating a sample along the propagation axis of a focused laser beam and monitoring the transmitted intensity as a function of the sample's position relative to the focal plane [61]. At positions far from focus, the intensity is low and nonlinear effects are negligible. As the sample moves closer to the focus, the intensity increases, giving rise to observable nonlinear behavior. For this investigation, a continuous-wave (CW) diode-pumped solid-state laser operating at 532 nm with an output power of 100 mW was employed. The laser beam, which had a Gaussian profile and operated in the TEM_{00} mode, was focused using a 130 mm focal length lens, resulting in a beam waist of 0.00293 cm. The Rayleigh range was determined to be 1.27 mm, and the peak intensity at the focal point reached approximately 14.78 kW/cm^2.

The MMB sample was prepared by dispersing the compound in double-distilled (DD) water, which served as the solvent. The solution was sonicated to ensure homogeneity and then taken in a 1 mm quartz cuvette for measurements. The linear transmittance of the sample at 532 nm was measured prior to the Z-scan study and found to be 98%, confirming negligible linear absorption. Importantly, we also verified that the NLO contribution of the solvent (DD water) under the same excitation conditions (532 nm, 0.01478 MW/cm^2) is negligible. This conclusion is supported by both direct measurement and established literature reports that show water exhibits near-zero third-order nonlinear susceptibility in the visible region. Furthermore, the linear refractive index (n_0) of the prepared solution was measured using an Abbe's refractometer (Na D line, 589 nm) at 32.7℃, confirming no anomalous effects were introduced by the solvent medium.

Under continuous-wave (CW) laser excitation at 532 nm, the nonlinear optical response of the MMB compound is predominantly governed by thermally induced mechanisms. Continuous photon absorption generates localized heating within the sample, producing a temperature gradient that modulates the refractive index through the thermal lensing effect, as originally reported by Sheik-Bahae et al. [62]. This thermally driven refractive index variation not only influences the nonlinear refraction but also enhances intensity-dependent absorption, leading to reverse saturable absorption (RSA), where the excited state absorption surpasses the ground-state absorption at higher intensities, consistent with previous studies [63]. The OA Z-scan traces obtained in this work confirm the RSA behavior, which accounts for the optical limiting properties observed in the MMB material. Overall, these thermal effects govern both the nonlinear refractive index (n_2) and the nonlinear absorption coefficient (β), thereby determining the effective third-order nonlinear optical susceptibility ($\chi^{(3)}$) under CW excitation.

Similar nonlinear effects have been reported in earlier studies, including the work of H. A. Badran et al., [64] where the nonlinear optical behavior of organic material was investigated using the Z-scan technique with a CW laser. In their study, thermal lensing played a key role in the observed nonlinear refraction, and the corresponding third-order nonlinear optical parameters were estimated based on the experimental data. Furthermore, H. Motiei et al. [65] provided a numerical and experimental analysis of thermal diffusion in CW Z-scan studies, confirming that thermal phase distortions strongly influence both OA and CA traces, and proposed to accurately extract thermally induced n_2 and β values for $\chi^{(3)}$ determination. Following these established approaches, the present study interprets the calculated n_2 and β values of the MMB compound as nonlinear coefficients, and these were subsequently used to estimate the magnitude of the effective third-order susceptibility $\chi^{(3)}$. These parameters are particularly relevant for evaluating the suitability of materials for low-power optical limiting and NLO applications.

Z-scan measurements of the MMB material were carried out in both open-aperture (OA) and closed-aperture (CA) configurations (Figs. 14a and b). The OA scan probes thermally induced nonlinear absorption, while the CA scan is sensitive to nonlinear refraction. The CA curve shows the combined effect of nonlinear refraction and absorption, whereas the CA/OA ratio removes the contribution of nonlinear absorption, allowing an accurate determination of the nonlinear refractive index **(n_2)** (see Fig. 14c) [66]. The valley observed in the OA trace indicates enhanced

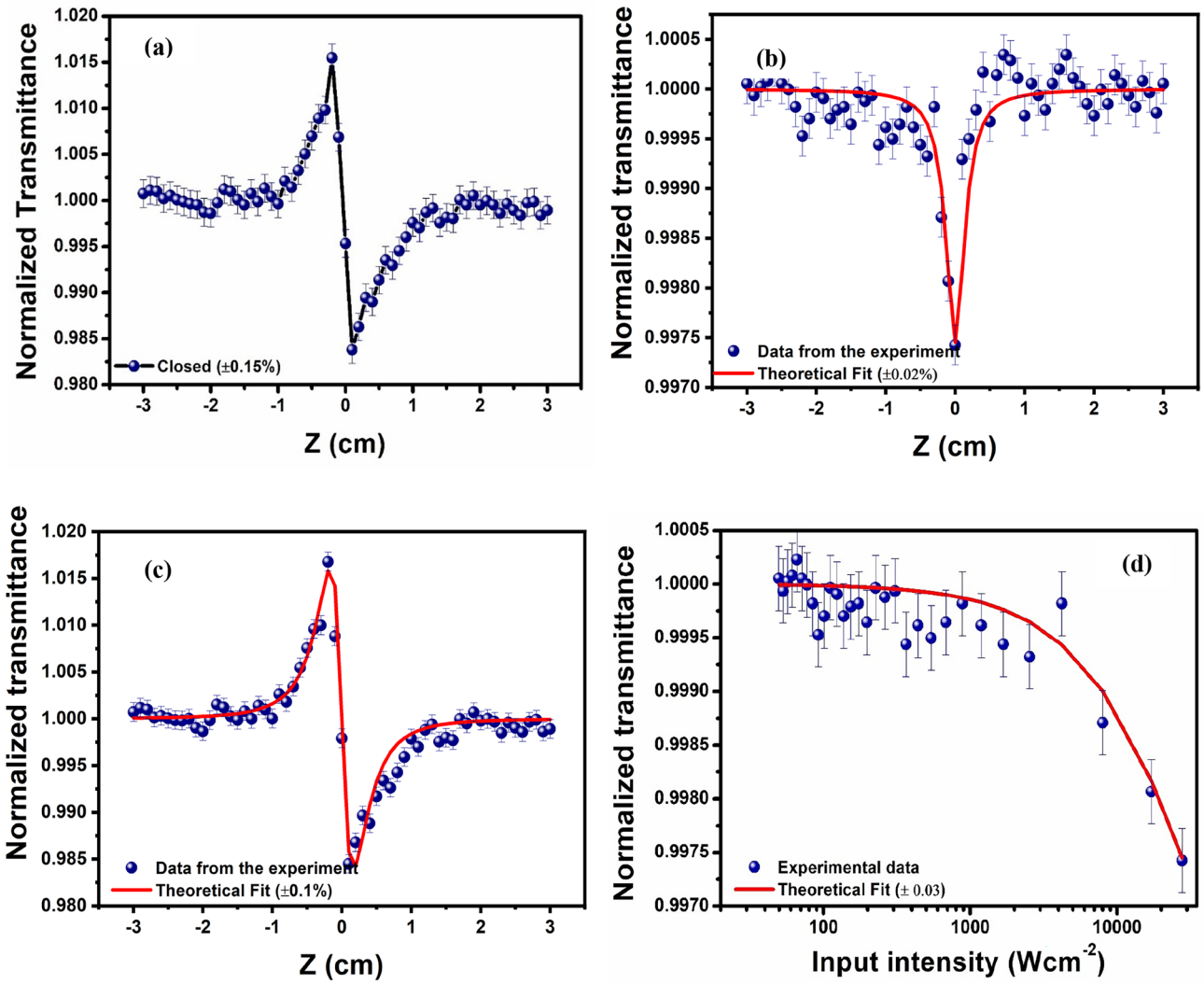

Fig. 14 (**a**) Closed, (**b**) open, (**c**) Ratio of closed to open-aperture Z-scan patterns and (**d**) optical limiting pattern of MMB

absorption at higher intensities, while the characteristic peak to valley pattern in the CA/OA ratio confirms a self-defocusing behavior, consistent with a negative n_2 arising from thermal effects [67]. The nonlinear refractive index was quantified by analyzing the transmittance difference between the peak and valley $\left(\Delta T_{p-v}\right)$ of the CA/OA ratio curve, which is mathematically related to the phase shift along the optical axis at the focal point, as described by the following equation;

$$|\Delta\phi| = \frac{\Delta T_{p-v}}{0.406(1-S)^{0.25}} \tag{6}$$

Here, S denotes the linear transmittance of the aperture, which is determined using below equation:

$$S = 1 - \exp\left(-\frac{2r_a^2}{\omega_a^2}\right) \tag{7}$$

In this formula, r_a denotes the aperture radius, while ω_a indicates the beam radius. The experimental data were fitted to a well-established Eq. (8) [68], yielding a $\Delta\phi$ value of 0.42 ± 0.001.

$$T_{CA} = \frac{4x\Delta\varphi}{(1+x^2)(9+x^2)} \tag{8}$$

Using the CA data, the n_2 was derived as follows:

$$n_2 = \frac{\Delta\varphi}{KI_0L_{eff}}, \tag{9}$$

where K, I_0 and L_{eff} represent the wave number, laser intensity, and sample effective thickness, respectively. The n_2 of MMB was found to be $(0.485 \pm 0.02)\times10^{-9}$ cm^2 W^{-1}. The nonlinear absorption coefficient (β) for the MMB compound was derived from the OA Z-scan results, and a theoretical fit was performed Eq. 11, demonstrating the presence of RSA. The calculation of β was performed using Eq. (10), as provided below.

$$\beta = \frac{2\sqrt{2}\Delta T}{I_0L_{eff}} \tag{10}$$

$$T_{OA} = \frac{1}{1+\left(\beta\times L_{eff}\left[\frac{I_0}{1+x^2}\right]\right)} \tag{11}$$

In the above equation, ΔT is the valley values in the OA curve. The computed β values of the MMB compound was determined to be $(0.0183 \pm 0.04)\times10^{-4}$ (cm/W). The connection between β and n_2 (nonlinear refractive index) is derived from the real and imaginary parts of the $\chi^{(3)}$, given by the following relationships [68]:

$$\chi_R^{(3)} = \frac{10^{-4}(\varepsilon_0c^2n_0^2n_2)}{\pi}\ (cm^2/W) \tag{12}$$

$$\chi_I^{(3)} = \frac{10^{-2}(\varepsilon_0c^2n_0^2\lambda\beta)}{4\pi^2}\ (cm/W) \tag{13}$$

Table 10 Comparison of $\chi^{(3)}$ values of MMB with reported nonlinear optical materials

Molecules	Third-order susceptibility ($\chi^{(3)}$)	References
MMB	3.06×10^{-8} esu	Present work
4AP4NP	1.80×10^{-8} esu	[35]
AMP4N	2.48×10^{-8} esu	[36]
VMST	9.69×10^{-12} esu	[69]
DMSB	1.60×10^{-8} esu	[70]
AAP	6.20×10^{-9} esu	[71]
4MSS	5.02×10^{-9} esu	[72]
DMPMS	3.12×10^{-12} esu	[73]
BTHBA	2.54×10^{-13} esu	[74]

Table 9 Third-order nonlinear optical parameters of MMB

Parameters	Values
Nonlinear refractive index (n_2)	$(0.485\pm0.02)\times10^{-9}$ cm^{2}W^{-1}
Nonlinear absorption coefficient (β)	$(0.0183\pm0.04)\times10^{-4}$ cmW^{-1}
Real part of third-order nonlinear optical susceptibility (Re (χ^3))	$(1.62\pm0.087)\times10^{-8}$ e.s.u.
Imaginary part of third-order nonlinear optical susceptibility (Im (χ^3))	$(2.59\pm0.06)\times10^{-8}$ e.s.u.
Third-order nonlinear optical susceptibility ($\chi^{(3)}$)	$(3.06\pm0.04)\times10^{-8}$ e.s.u.

where λ, n_0, c, and ε_0 are the universal constant. The magnitude of the $\chi^{(3)}$ is then calculated as:

$$\chi^{(3)} = \sqrt{\left(\chi_R^{(3)}\right)^2 + \left(\chi_I^{(3)}\right)^2}\ (e.s.u.) \tag{14}$$

The calculated $\chi^{(3)}$ value, along with other NLO parameters (n_2 and β) are summarized in Table 9. The obtained $\chi^{(3)}$ value of MMB is compared with other reported NLO materials [35, 36, 69–74] under CW excitation at 532 nm, as listed in Table 10. The comparison shows that MMB exhibits a relatively high $\chi^{(3)}$ value (3.06×10^{-8} e.s.u.), demonstrating a strong third-order nonlinear response compared to the other NLO materials. This study highlights the competitive NLO performance of MMB, which can be attributed to its molecular structure and thermal lensing effects under CW excitation, emphasizing its potential for optical limiting and other third-order NLO applications [75].

3.9.2 Optical limiting (OL) study

The increasing integration of lasers in modern technologies has led to a growing need for devices capable of protecting sensitive optical systems from damaging laser intensities. Such devices, known as optical limiters, are crucial for safeguarding components. Materials exhibiting RSA properties are particularly suitable for OL applications. In this study, we investigated the OL performance of the MMB compound using open-aperture (OA) Z-scan data under continuous-wave (CW) laser excitation. A significant reduction in transmittance was observed near the focal point (Z = 0), indicating a strong nonlinear absorption response. This reduction is attributed to thermally induced effects—specifically, localized heating due to continuous light absorption, which enhances the material's absorption and leads to a decrease in transmitted intensity. These thermal effects resemble RSA behavior and are effective for OL applications under CW conditions.

To evaluate the variation in beam intensity along the optical axis, the position-dependent intensity I(z) was computed using the following equation:

$$I(z) = 4\sqrt{\ln 2}\left(\frac{E_{in}}{\pi^{3/2}\omega(z)^2}\right) \tag{15}$$

where $\omega\ (z) = \omega_0^2\ [1 + (z/z_0)^2$ is being a beam radius. The OL curves for the MMB sample are illustrated in Fig. 14(d). The OL threshold values were established under continuous-wave (CW) excitation, resulting in $(3.906 \pm 0.03)\times10^3$ Wcm^{-2}, which further emphasizes the material's suitability for OL applications. Recent studies have utilized the Z-scan method via CW laser conditions at 532 nm have reported similar optical limiting (OL) properties. For instance, S. Pratheba et al. reported threshold values of 3.44×10^3 Wcm^{-2} for 4MPB [76], and Ananda et al. found values of 3.437×10^3 Wcm^{-2} for BCA [39]. The threshold value of our MMB compound is consistent with these findings, indicating its strong potential for OL applications.

Table 11 Dipole moment, static and dynamic polarizability by TDHF at 6–311++G(d,p) of MMB

Dipole moment (μ)		Polarizability (α)			
Components	Values (Debye)	Components	ω = 0	ω = 0.04282 λ = 1064 nm	ω = 0.08564 λ = 532 nm
μ_x	− 2.058	α_{xx}	266.20	272.75	296.82
μ_y	− 6.859	α_{xy}	168.73	170.29	175.32
μ_z	0.444	α_{yy}	72.72	72.96	73.69
		α_{xz}	− 4.21	− 4.52	− 5.67
μ_{total}	7.175	α_{yz}	2.02	2.06	2.18
		α_{zz}	12.87	13.04	13.59
		α_{total} a.u	169.21	172.00	181.95
		$\alpha_{total}\times10^{-23}$esu	2.53	2.58	2.72
		Δα a.u	426.29	433.67	460.21
		$\Delta\alpha\times10^{-23}$ esu	6.39	6.50	6.90

Table 12 The static and dynamic first-order hyperpolarizability by TDHF/6–311++G(d,p) level

Components	ω = 0	ω = 0.04282 λ = 1064 nm	ω = 0.08564 λ = 532 nm
β_{xxx}	− 10.64	− 2.45	956.0
β_{xyy}	26.84	17.65	− 480.36
β_{xzz}	0.94	− 4.03	− 169.81
β_{yyy}	55.17	59.02	98.92
β_{yzz}	21.75	23.07	36.46
β_{yxx}	− 183.80	− 229.69	− 578.49
β_{zzz}	− 11.46	− 11.77	− 13.42
β_{zxx}	− 23.18	− 28.78	− 61.12
β_{zyy}	10.47	− 22.09	62.45
β_{x}	294.06	124.40	93,561.71
β_{y}	11,422.65	21,782.42	196,343.81
β_{z}	584.21	887.11	4233.64
β a.u	110.90	150.97	542.34
$\beta \times 10^{-30}$ esu	0.95	1.30	4.68

Table 13 The static second hyperpolarizability γ(0;0,0,0) and frequency-dependent second hyperpolarizability γ(−3ω;ω, ω, ω) at 6–311++G(d,p)) method (TDHF)

Components	ω = 0	ω = 0.04282 λ = 1064 nm	ω = 0.08564 λ = 532 nm
γ_{xxxx}	147,639.20	317,790.80	3,406,277
γ_{yyyy}	5404.79	6531.12	36,414.49
γ_{zzzz}	490.96	560.61	1117.54
γ_{xxyy}	6118.03	11,180.08	14,865.99
γ_{xxzz}	485.58	915.58	− 7407.81
γ_{yyzz}	460.74	588.23	5465.83
γ a.u	33,532.73	70,050.05	693,931.36
$\gamma \times 10^{-36}$ esu	16.90	35.30	349.74

3.9.3 *Theoretical NLO studies*

Computational techniques play a crucial role in investigating the NLO properties of complex molecular structures, enabling the prediction of their behavior under various electromagnetic fields. Methods such as TDHF and DFT provide accurate calculations of key NLO parameters, including polarizability (α), first hyperpolarizability (β), and second hyperpolarizability (γ) [77]. These theoretical approaches not only complement experimental findings but also elucidate molecular interactions and charge transfer processes that govern NLO behavior [78]. As the demand for advanced photonic materials grows, computational NLO research identifies promising candidates for applications in optoelectronics and telecommunications [79]. In this study, we investigate the NLO characteristics of the MMB molecule using the TDHF method within the GAMESS software suite. Using the 6–311++G(d, p) basis set, we conduct calculations at various frequencies to determine α, β, and γ at various frequencies ($\omega = 0$, 0.04282 and 0.08564 a.u). Detailed results are present in Tables 11, 12, and 13. The results reveal that all tensor components demonstrated non-zero values in specific spatial directions. Notably, the x-axis components such as α_{xx}, β_{xxx}, and γ_{xxxx}, emerged as the most prominent contributors, especially for longitudinal measurements. These dominant values provide evidence of a charge transfer mechanism along the x-direction in the MMB molecule. The molecule's donor–acceptor configuration significantly influenced the dipole moment, which was calculated to be 7.175 Debye.

The static polarizability at $\omega = 0$ a.u. was calculated using the tensor components along the x, y, and z axes. Dynamic polarizability was further calculated at two different frequencies: 0.04282 a.u. and 0.08564 a.u., with the results summarized in Table 11. The static polarizability values (α_{total} and $\Delta\alpha$) were determined to be 2.53×10^{-23} e.s.u. and 6.39×10^{-23} e.s.u., respectively. Additionally, the dynamic values for α_{total} and $\Delta\alpha$ at 0.04282 a.u. were found to be 2.58×10^{-23}, and 6.50×10^{-23} e.s.u., while at 0.08564 a.u., they were found to be 2.72×10^{-23}, and 6.90×10^{-23}. The orientation-averaged isotropic and anisotropic values, along with the responses of all tensor components, exhibit an increasing with increased input frequency. Notably, the dynamic polarizability values exceed the corresponding static values, indicating that the molecule's polarizability is influenced by the applied electromagnetic field. This observation underscores the frequency-dependent nature of molecular polarizability [80].

In MMB molecule, the increase in ICT and resonance interactions leads to a pronounced amplification of their NLO response, resulting in a considerable enhancement of second-order nonlinearity (β). As shown in Table 12, the static first hyperpolarizability $\beta(0;0,0)$ is calculated to be 0.9583×10^{-30} while the dynamic first hyperpolarizability $\beta(-2\omega;\omega,\omega)$ is evaluated at two different frequecncies: 1.30×10^{-30} e.s.u. at $\omega = 0.04282$ a.u, and 4.68×10^{-30} e.s.u. at $\omega = 0.08564$ a.u. and

these values are 1.76 and 6.36 times higher than the urea (0.73512×10^{-30} e.s.u.) [81], respectively. The second-order hyperpolarizability components of the MMB molecule, both static and dynamic, have been calculated at different frequencies, and the results are presented in Table 13. These molecular gamma (γ) values depend on several factors such as π-electron delocalization, molecular structure, and the type of substituents. The MMB molecule's donor–acceptor π-conjugated system enables charge transfer through the phenyl rings, thereby impacting its nonlinear optical properties. The phenyl rings act as essential intermediaries, especially in the presence of donor–acceptor substituents, leading to non-zero static and dynamic hyperpolarizabilities, which reflect the molecule's NLO behavior on a microscopic scale [81]. The MMB's computed value of $\gamma(0;\ 0,\ 0,\ 0)$ was determined to be 20.865×10^{-36} e.s.u. Additionally, the dynamic $\gamma\ (3\omega;\ \omega,\ \omega,\ \omega)$ was evaluated at two distinct frequencies (0.04282 a.u. and 0.08564 a.u.), yielding values of 35.30×10^{-36} e.s.u. and 349.74×10^{-36} e.s.u., respectively. From the Tables 12 and 13, it is noted that as the input frequency decreases, the first and second hyperpolarizability components within the MMB molecule also decrease. Overall the findings suggest that the studied molecule holds promise for nonlinear optical (NLO) applications.

4 Conclusion

In summary, the MMB crystal, a novel organic compound, was synthesized through the reflux method, and its structural and spectroscopic characteristics were thoroughly characterized by NMR and single-crystal XRD. Structural analysis confirmed that MMB crystallizes in the $P2_1/c$ space group. MMB's optical studies reveal that the studied crystals display significant transparency (98%) and minimal absorption throughout the visible spectrum, with a cut-off observed at 331 nm. Additionally, the optical band gap (E_g) was determined to be 3.48 eV via Tauc's plot from the UV–Vis spectra. Photoluminescence results show that MMB emits blue light, underscoring its potential as a promising candidate for blue LED applications. The solvatochromic studies showed that nonpolar solvents exhibit higher values of α_{CT}, β_{CT}, and γ_{CT} compared to polar solvents. In the MMB compound in acetonitrile solvent, these values were found to be 3.40×10^{-24}, 2.21×10^{-28}, and 1.28×10^{-32} e.s.u. Thermogravimetric analysis (TGA) indicated that the studied compound remains thermally stable up to 188.89℃. The calculated HOMO–LUMO energy gap (E_g = 4.148 eV) indicates enhanced ICT interactions within the MMB molecule. Additionally, the GCRD measurements reveal a significant hardness value of 2.074 eV, suggesting the molecule's stability and low chemical reactivity. Natural Bond Orbital (NBO) analysis identified that the most prominent interaction arises from the intramolecular charge transfer (ICT) between lone pairs on (N8) and π* (C7–O16) bond, with stabilization energy of 46.14 kJ/mol. QTAIM and NCI analyses confirmed the presence of noncovalent interactions, including hydrogen bonds and van der Waals forces. The Z-scan results demonstrate that the MMB compound exhibits both RSA and self-defocusing behavior under CW laser irradiation. The MMB compound's OL value ($(3.906\pm0.03)\times10^3$ Wcm^{-2}) further highlights its potential for OL applications. Additionally, the MMB's first and second hyperpolarizability values suggest strong NLO behavior. Collectively, these findings underscore MMB as a promising material for use in photonic devices, NLO device fabrication, and electro-optical technologies.

Acknowledgements

The author Keerthikumara V thanks to University Grants Commission (UGC), New Delhi for providing financial support (NTA-Ref. No.: 201610078208, Dated: 01-04-2021). The authors would like to thank the University with Potential for Excellence (UPE) University of Mysore for providing UV-Vis measurements and also thank SAIF, IIT-Madras for single-crystal XRD analysis. We express our gratitude to Dr. Jeyaseelan S. for granting us access to the computational facility. Dr. Mahendra M would like to thank VGST, Government of Karnataka for awarding a research grant under the head K-FIST L2 (KSTePS/VGST/GRD No. 1133/2022–23/654).

Author contributions

V. Keerthikumara: Writing– review & editing, Writing original draft, Visualization, Validation, Software,

Resources, Method ology, Investigation, Formal analysis, Data curation, Conceptualization. H. Keshav Kumar: Software, Investigation, Resources, Formal analysis. M. Vindu Vahini: Software, Methodology, Investigation, Formal analysis, Data curation. H. M. Bhanu Prakash: Software, Resources, Formal analysis. N. R. Bhavya: Formal analysis, Data curation. Samyukta Ram Mohan: Data curation, Software. Tejaswi Ashok Hegde: Software, Methodology, Formal analysis, Data curation. M. Mahendra: Writing– review & editing, Supervision, Software, Methodology, Formal analysis, Conceptualization.

Funding

The authors have not disclosed any funding.

Data availability

The data that support the findings of this study are available on request from the corresponding author.

Declarations

Conflict of interest The authors declare that they have no known competing financial interests or personal relationships that could have appeared to influence the work reported in this paper.

Supplementary Information The online version contains supplementary material available at https://doi.org/10.1007/s10854-025-16018-w.

References

1. F.W. Gao, H. Xu, Z.M. Su, Tuning the inter-molecular charge transfer, second-order nonlinear optical and absorption spectra properties of a π-dimer under an external electric field. Phys. Chem. Chem. Phys. **19**(47), 31958–31964 (2017). https://doi.org/10.1039/C7CP06412H
2. V. G. Dmitriev, G. G. Gurzadyan, D. N. Nikogosyan, Handbook of nonlinear optical crystals. **64**, Springer (2013).
3. M. Gryl, T. Seidler, J. Wojnarska, K. Stadnicka, I. Matulková, I. Němec, P. Němec, Co-crystals of 2-amino-5-nitropyridine barbital with extreme birefringence and large second harmonic generation effect. Chem. Eur. J. **24**(35), 8727–8731 (2018). https://doi.org/10.1002/chem.201802057
4. O. Diels, The Diels-alder reaction. Ber. Dtsch. Chem. Ges. **62**, 554–562 (1929)
5. J. Wu, J. Luo, A.K.Y. Jen, High-performance organic second-and third-order nonlinear optical materials for ultrafast information processing. J. Mater. Chem. C. **8**(43), 15009–15026 (2020). https://doi.org/10.1039/D0TC03224G
6. J.L. Segura, M.J. Mancheño, F. Zamora, Covalent organic frameworks based on Schiff-base chemistry: synthesis, properties and potential applications. Chem. Soc. Rev. **45**(20), 5635–5671 (2016). https://doi.org/10.1039/C5CS00878F
7. A.D. Naik, Gl. Fontaine, S. Bellayer, S. Bourbigot, Crossing the traditional boundaries: Salen-based Schiff bases for thermal protective applications. ACS Appl. Mater. Interfaces **7**(38), 21208–21217 (2015). https://doi.org/10.1021/acsami.5b05164
8. N.E. Kassan, H.A. Saadeh, W.H. Talib, A.M. Mahasneh, H. Kaur, K. Goyal, R. Sehgal, M.S. Mubarak, Synthesis and biological activity of novel Schiff bases derived from metronidazole. Med. Chem. Res. **23**, 4872–4882 (2014). https://doi.org/10.1007/s00044-014-1055-4
9. I.H.A. Ripain, N. Ngah, A brief review on the thiazole derivatives: synthesis methods and biological activities. Malays. J. Anal. Sci. **25**, 257–267 (2021)
10. B. Maji, S. Debnath, T. Panda, A. Manna, R. Maity, R. Dayaramani, R. Nath, S.A. Khan, M.J. Akhtar, Anticancer potential of the S-heterocyclic ring containing drugs and its bioactivation to reactive metabolites. Chem. Biodivers. **21**(7), 202400473 (2024). https://doi.org/10.1002/cbdv.202400473
11. K. Venkatesha, K. Sheela, M.S. Srinivas, A. Swamynayaka, M. Madegowda, T.A. Hegde, M.P. Sadashiva, Physicochemical properties of thiazole-based NLO crystal: an efficient material for optoelectronic applications. J. Mol. Struct. **1319**, 139459 (2025). https://doi.org/10.1016/j.molstruc.2024.139459
12. S. Bradamante, A. Facchetti, G.A. Pagani, Heterocycles as donor and acceptor units in push–pull conjugated molecules Part 1. J. Phys. Org. Chem. **10**, 514–524 (1997). https://doi.org/10.1002/(SICI)1099-1395(199707)10:7%3c514::AID-POC897%3e3.0.CO;2-J
13. A. Facchetti, A. Abbotto, L. Beverina, M.E. Van Der Boom, P. Dutta, G. Evmenenko, T.J. Marks, G.A. Pagani, Azinium−(π-bridge)− pyrrole NLO-phores: influence of heterocycle acceptors on chromophoric and self-assembled thin-film properties. Chem. Mater. **14**(12), 4996–5005 (2002). https://doi.org/10.1021/cm0205635

14. A. Facchetti, L. Beverina, M.E. Van Der Boom, P. Dutta, G. Evmenenko, A.D. Shukla, C.E. Stern, G.A. Pagani, T.J. Marks, Strategies for electrooptic film fabrication. Influence of pyrrole−pyridine-based dibranched chromophore architecture on covalent self-assembly, thin-film microstructure, and nonlinear optical response. J. Am. Chem. Soc. **128**(6), 2142–2153 (2016). https://doi.org/10.1021/ja057556c
15. M. Haroon, M. Khalid, T. Akhtar, M.N. Tahir, M.U. Khan, S. Muhammad, A.G. Al-Sehemi, S. Hameed, Synthesis, crystal structure, spectroscopic, electronic and nonlinear optical properties of potent thiazole based derivatives: joint experimental and computational insight. J. Mol. Struct. **1202**, 127354 (2020). https://doi.org/10.1016/j.molstruc.2019.127354
16. M.M.M. Raposo, M.C.R. Castro, A.M.C. Fonseca, P. Schellenberg, M. Belsley, Design, synthesis, and characterization of the electrochemical, nonlinear optical properties, and theoretical studies of novel thienylpyrrole azo dyes bearing benzothiazole acceptor groups. Tetrahedron **67**(29), 5189–5198 (2011). https://doi.org/10.1016/j.tet.2011.05.053
17. A. Nekrouf, K. Toubal, Y. Megrouss, N.E.H. Belkafouf, A. Djafri, N. Khelloul, J.-C. Daran, A. Djafri, A. Chouaih, Synthesis, structural, spectroscopic, intermolecular interactions, kinetic stability, charge transfer method with DNA bases and electronic properties of (E)-3-(2-ethoxyphenyl)-5-(3-(2-methoxyphenyl)-4methylthiazol-2 (3H)-ylidene)-2-thioxothiazolidin-4-one: Computational and experimental approach. J. Mol. Struct. **1262**, 133002 (2022). https://doi.org/10.1016/j.molstruc.2022.133002
18. V.V. Salian, B. Narayana, B.K. Sarojini, M.S. Kumar, G.S. Nagananda, K. Byrappa, A.K. Kudva, Spectroscopic, single crystal X-ray, Hirshfeld, in vitro and in silico biological evaluation of a new series of potent thiazole nucleus integrated with pyrazoline scaffolds. Spectrochim. Acta A Mol. Biomol. Spectrosc. **174**, 254–271 (2017). https://doi.org/10.1016/j.saa.2016.11.046
19. P.G. More, N.N. Karale, A.S. Lawand, N. Narang, R.H. Patil, Synthesis and anti-biofilm activity of thiazole Schiff bases. Med. Chem. Res. **23**, 790–799 (2014). https://doi.org/10.1007/s00044-013-0672-7
20. A.D.A. Sykula, Schiff bases as important class of pharmacological agents. J. Pharm. Pharmacol. **6**, 989–1009 (2018)
21. H.H. Radamson, X-ray techniques, in *Analytical methods and instruments for micro- and nanomaterials*. (Springer International Publishing, Cham, 2023), pp.3–53
22. G.M. Sheldrick, Crystal structure refinement with SHELXL. Acta Crystallogr. C Struct. Chem. **71**, 3–8 (2015). https://doi.org/10.1107/S2053229614024218
23. C.F. Macrae, I. Sovago, S.J. Cottrell, P.T.A. Galek, P. McCabe, E. Pidcock, M. Platings, G.P. Shields, J.S. Stevens, M. Towler, P.A. Wood, Mercury 4.0: from visualization to analysis, design and prediction. J. Appl. Crystallogr. **53**, 226–235 (2020). https://doi.org/10.1107/S1600576719014092
24. A.L. Spek, Single-crystal structure validation with the program PLATON. J. Appl. Crystallogr. **36**, 7–13 (2003). https://doi.org/10.1107/S0021889802022112
25. M. Frisch, G. Trucks, H. Schlegel, G. Scuseria, M. Robb, J. Cheeseman, G. Scalmani, V. Barone, B. Mennucci, G. Petersson, *Gaussian 09* (Gaussian, Inc., Wallingford, CT, 2009)
26. T. Lu, F. Chen, Multiwfn: a multifunctional wavefunction analyzer. J. Comput. Chem. **33**, 580–592 (2012). https://doi.org/10.1002/jcc.22885
27. W. Humphrey, A. Dalke, K. Schulten, VMD: visual molecular dynamics. J. Mol. Graph. **14**, 33–38 (1996). https://doi.org/10.1016/0263-7855(96)00018-5
28. H.A. Kurtz, J.J. Stewart, K.M. Dieter, Calculation of the nonlinear optical properties of molecules. J. Comput. Chem. **11**, 82–87 (1990). https://doi.org/10.1002/jcc.540110110
29. H.A. Khamees, K. Chaluvaiah, N.A. El-Khatatneh, A. Swamynayaka, K.H. Chong, J.P. Dasappa, M. Madegowda, Crystal structure, DFT calculation, Hirshfeld surface analysis and energy framework study of 6-bromo-2-(4-bromophenyl)imidazo[1,2-a]pyridine. Acta Crystallogr. Sect. E Crystallogr. Commun. **75**, 1620–1626 (2019). https://doi.org/10.1107/S2056989019013410
30. F. Güntepe, H. Saraçoğlu, N. Çalıskan, Ç. Yüksektepe, A. Çukurovalı, Structure and DFT calculations of 2-{[3-methyl-3-phenyl-cyclobutyl)-thiazol-2-yl]-hydrazonomethyl}-phenol. J. Struct. Chem. **52**, 596–601 (2011). https://doi.org/10.1134/S002247661103022X
31. J. Tauc, A. Menth, States in the gap. J. Non-Cryst. Solids **8**, 569–585 (1972). https://doi.org/10.1016/0022-3093(72)90194-9
32. A. Dolgonos, T.O. Mason, K.R. Poeppelmeier, Direct optical band gap measurement in polycrystalline semiconductors: a critical look at the Tauc method. J. Solid State Chem. **240**, 43–48 (2016). https://doi.org/10.1016/j.jssc.2016.05.010
33. P. Makuła, M. Pacia, W. Macyk, How to correctly determine the band gap energy of modified semiconductor photocatalysts based on UV–Vis spectra. J. Phys. Chem. Lett. **9**, 6814–6817 (2018). https://doi.org/10.1021/acs.jpclett.8b02892
34. T.S. Girisun, S. Dhanuskodi, Linear and nonlinear optical properties of tris thiourea zinc sulphate single crystals.

Cryst. Res. Technol. **44**, 1297–1302 (2009). https://doi.org/10.1002/crat.200900351

35. T. Kamalesh, P. Karuppasamy, M. Senthil Pandian, P. Ramasamy, S. Verma, Synthesis, crystal growth, and physicochemical characterization of 4-aminopyridinium 4-nitrophenolate 4-nitrophenol (4AP4NP) single crystals for NLO applications. J. Mater. Sci. Mater. Electron. **32**, 6141–6157 (2021). https://doi.org/10.1007/s10854-021-05332-8
36. P. Karuppasamy, T. Kamalesh, K. Anitha, S.A. Kalam, M.S. Pandian, P. Ramasamy, S.V. Rao, Synthesis, crystal growth, structure and characterization of a novel third-order nonlinear optical organic single crystal: 2-amino 4,6-dimethyl pyrimidine 4-nitrophenol. Opt. Mater. **84**, 475–489 (2018). https://doi.org/10.1016/j.optmat.2018.07.039
37. G.A. Nowsherwan, Q. Ali, U.F. Ali, M. Ahmad, M. Khan, S.S. Hussain, Advances in organic materials for next-generation optoelectronics: potential and challenges. Organics **5**, 520–560 (2024). https://doi.org/10.3390/org5040028
38. H. Purandara, S. Raghavendra, S. Foro, P. Patil, B.T. Gowda, S.M. Dharmaprakash, P. Vishwanatha, Synthesis, spectroscopic characterization, crystal structure, Hirshfeld surface analysis and third-order nonlinear optical properties of 2-(4-chlorophenoxy)-N'-[(1E)-1-(4-methylphenyl) ethylidene]acetohydrazide. J. Mol. Struct. **1185**, 205–211 (2019). https://doi.org/10.1016/j.molstruc.2019.02.079
39. A. Swamynayaka, K. Venkatesha, K.K. Harish, B.N. Revanna, C. Venkatesh, M. Madegowda, T.A. Hegde, Third-order nonlinear response of a novel organic acetohydrazide derivative: experimental and theoretical approach. Opt. Mater. **139**, 113826 (2023). https://doi.org/10.1016/j.optmat.2023.113826
40. S. Raghavendra, C.S. Chidankumar, A. Jayarama, S.M. Dharmaprakash, Mater. Chem. Phys. (2015). https://doi.org/10.1016/j.matchemphys.2014.10.050
41. A. Priyadharshini, S. Kalainathan, Synthesis, structure and characterization of new promising organic NLO crystal: thiosemicarbazide 4-hydroxybenzenesulfonate monohydrate (THBSM). J. Mater. Sci. Mater. Electron. **28**(10), 7401–7412 (2017). https://doi.org/10.1007/s10854-017-6429-1
42. M. Shankar, A.D. Raj, M. Jeeva, R. Purusothaman, M. Vimalan, I.V. Potheher, Synthesis, crystal growth, thermal and laser damage threshold properties of new Schiff base NLO material 4-nitro-benzoic acid (3-ethoxy-2-hydroxy-benzylidene)-hydrazide. Mater. Lett. **232**, 113–117 (2018). https://doi.org/10.1016/j.matlet.2018.08.090
43. C. Reichardt, T. Welton, *Solvents and solvent effects in organic chemistry* (John Wiley & Sons, Hoboken, 2010)
44. P. Suppan, Excited-state dipole moments from absorption/fluorescence solvatochromic ratios. Chem. Phys. Lett. **94**, 272–275 (1983). https://doi.org/10.1016/0009-2614(83)87086-9
45. M. Homocianu, Exploring solvatochromism: a comprehensive analysis of research data. Microchem. J. **198**, 110166 (2024). https://doi.org/10.1016/j.microc.2024.110166
46. S. Nadeem, A. Anwar, M.U. Khan, A.U. Hassan, K.A. Alrashidi, Synergistic charge-transfer dynamics of novel pyridoquinazolindone-containing triphenylamine-based push–pull chromophores: from structural optimization to performance metrics in photovoltaic solar cells and static, dynamic, solvent-dependent nonlinear optical response applications. RSC Adv. **14**, 32482–32500 (2024). https://doi.org/10.1039/D4RA05290K
47. A. Raiol, M. Pinheiro, E. Belo, A.R. da Cunha, A.M. Marinho, S.Y. Silva, R. Gester, Experimental and theoretical spectroscopic characterization, NLO response, and reactivity of the pharmacological agent spilanthol and analogues. J. Mol. Struct. **1227**, 129423 (2021). https://doi.org/10.1016/j.molstruc.2020.129423
48. M. Ashfaq, M.N. Tahir, S. Muhammad, K.S. Munawar, A. Ali, G. Bogdanov, S.S. Alarfaji, Single-crystal investigation, Hirshfeld surface analysis, and DFT study of third-order NLO properties of unsymmetrical acyl thiourea derivatives. ACS Omega **6**, 31211–31225 (2021). https://doi.org/10.1021/acsomega.1c04884
49. A. Gavezzotti, *Molecular aggregation: structure analysis and molecular simulation of crystals and liquids*, vol. 19 (OUP Oxford, Oxford, 2007)
50. P.R. Spackman, M.J. Turner, J.J. McKinnon, S.K. Wolff, D.J. Grimwood, D. Jayatilaka, M.A. Spackman, Crystalexplorer: a program for Hirshfeld surface analysis, visualization and quantitative analysis of molecular crystals. Acta Crystallogr. A **54**, 1006–1011 (2021). https://doi.org/10.1107/S1600576721002910
51. M.A. Spackman, J.J. McKinnon, Fingerprinting intermolecular interactions in molecular crystals. CrystEngComm **4**, 378–392 (2002). https://doi.org/10.1039/B203191B
52. C. Shruthi, V. Ravindrachary, B. Guruswamy, D.J. Prasad, J. Goveas, K. Kumara, N.K. Lokanath, Molecular structure, Hirshfeld surface and density functional theoretical analysis of a NLO active chalcone derivative single crystal—a quantum chemical approach. J. Mol. Struct. **1228**, 129739 (2021). https://doi.org/10.1016/j.molstruc.2020.129739
53. A.E. Reed, R.B. Weinstock, F. Weinhold, Natural population analysis. J. Chem. Phys. **83**, 735–746 (1985). https://doi.org/10.1063/1.449486
54. D.A. Zainuri, M.F. Zaini, S.N.F. Ab Rahman, M.A.A. Bakar, S.N.A.M. Nizar, M. Abdullah, S. Arshad,

Heterocyclic chalcone derivatives with D-π-A framing modulated electronic, linear and nonlinear optical properties as effective candidates for nonlinear optical applications. Phys. B **650**, 414573 (2023). https://doi.org/10.1016/j.physb.2022.414573

55. K.K. Harish, A.R. Nesaragi, N.K. Kalagatur, P. Naik, M. Madegowda, A. Pandith, H. Guddappa, Imidazole-centred cupric ions sensor: experimental validation, theoretical understanding, and zebrafish bioimaging. J. Photochem. Photobiol. A Chem. **452**, 115565 (2024). https://doi.org/10.1016/j.jphotochem.2024.115565
56. K. Fukui, N. Koga, H. Fujimoto, Interaction frontier orbitals. J. Am. Chem. Soc. **103**, 196–197 (1981). https://doi.org/10.1021/ja00391a039
57. R.G. Parr, R.G. Pearson, Absolute hardness: companion parameter to absolute electronegativity. J. Am. Chem. Soc. **105**, 7512–7516 (1983). https://doi.org/10.1021/ja00364a005
58. M. Leboeuf, A.M. Köster, K. Jug, D.R. Salahub, Topological analysis of the molecular electrostatic potential. J. Chem. Phys. **111**, 4893–4905 (1999). https://doi.org/10.1063/1.479749
59. S. Emamian, T. Lu, H. Kruse, H. Emamian, Exploring nature and predicting strength of hydrogen bonds: a correlation analysis between atoms-in-molecules descriptors, binding energies, and energy components of symmetry-adapted perturbation theory. J. Comput. Chem. **40**, 2868–2881 (2019). https://doi.org/10.1002/jcc.26068
60. M. Essid, S. Muhammad, H. Marouani, A. Saeed, Z. Aloui, A.G. Al-Sehemi, Synthesis, characterization, Hirshfeld surface analysis and computational studies of 1-methylpiperazine-1,4-diium bis(hydrogen oxalate): $[C_5H_{14}N_2](HC_2O_4)_2$. J. Mol. Struct. **1211**, 128075 (2020). https://doi.org/10.1016/j.molstruc.2020.128075
61. T.A. Hegde, T.S. Girisun, G. Vinitha, Crystal structure and physicochemical properties of a new optofunctional metal-organic cocrystal delivering intermolecular charge-transfer-enhanced nonlinear optical and optical limiting properties. J. Mater. Sci. Mater. Electron. **32**, 18669–18688 (2021). https://doi.org/10.1007/s10854-021-06364-w
62. M. Sheik-Bahae, A.A. Said, E.W. Van Stryland, High-sensitivity, single-beam n_2 measurements. Opt. Lett. **14**, 955–957 (1989). https://doi.org/10.1364/OL.14.000955
63. C. Yogeswari, K.M. Hijas, T.S. Girisun, R. Nagalakshmi, Intensity dependent nonlinear absorption switching behavior of electrospun meta-nitroaniline nanofiber. Opt. Mater. **100**, 109691 (2020). https://doi.org/10.1016/j.optmat.2020.109691
64. H.A. Badran, A.A. Al-Fregi, R.F. Alfahed, A.S. Al-Asadi, Study of thermal lens technique and third-order nonlinear susceptibility of PMMA base containing 5′,5′′-dibromo-o-cresolsulfophthalein. J. Mater. Sci. Mater. Electron. **28**, 17288–17296 (2017). https://doi.org/10.1007/s10854-017-7661-4
65. H. Motiei, A. Jafari, R. Naderali, Third-order nonlinear optical properties of organic azo dyes by using strength of nonlinearity parameter and Z-scan technique. Opt. Laser Technol. **88**, 68–74 (2017). https://doi.org/10.1016/j.optlastec.2016.09.011
66. N. Priyadarshani, G. Vinitha, T.S. Girisun, Third-order nonlinear optical properties of monoclinic and orthorhombic $CuNb_2O_6$ under CW laser illumination. Opt. Laser Technol. **108**, 287–294 (2018). https://doi.org/10.1016/j.optlastec.2018.06.040
67. T.S. Girisun, S. Dhanuskodi, G. Vinitha, χ^3 measurement and optical limiting properties of metal complexes of thiourea using Z-scan. Mater. Chem. Phys. **129**, 9–14 (2011). https://doi.org/10.1016/j.matchemphys.2011.04.013
68. M. Sheik-Bahae, A.A. Said, T.H. Wei, D.J. Hagan, E.W. Van Stryland, Sensitive measurement of optical nonlinearities using a single beam. IEEE J. Quantum Electron. **26**, 760–769 (2002)
69. M.K. Kumar, S. Sudhahar, P. Pandi, G. Bhagavannarayana, R.M. Kumar, Studies of the structural and third-order nonlinear optical properties of solution grown 4-hydroxy-3-methoxy-4′-N′-methylstilbazolium tosylate monohydrate crystals. Opt. Mater. **36**, 988–995 (2014). https://doi.org/10.1016/j.optmat.2014.01.007
70. R. Vinayagamoorthy, M.U. Rani, S. Kalainathan, S. Anand, A novel stilbazolium derivative crystals of 4-[2-(4-dimethyl amino-phenyl)-vinyl]-1-methyl-pyridinium+ bromide−(DMSB) single crystal: exploration of the growth, molecular structure, linear optical, and third order nonlinear properties. RSC Adv. **13**, 24867–24877 (2023). https://doi.org/10.1039/D3RA04322C
71. A. Arunkumar, P. Ramasamy, Bulk single crystals of ammonium acid phthalate grown by the Sankaranarayanan-Ramasamy method for optical limiting applications. J. Cryst. Growth **401**, 195–199 (2014). https://doi.org/10.1016/j.jcrysgro.2013.10.049
72. D. Shalini, S. Kalainathan, N. Hema, R. Usha, D. Jayalakshmi, Synthesis, growth and broadband dielectric characterization of nonlinear optical single crystal: 4-methylpyridinium5-sulfosalicylate. Mater. Res. Innov. **23**, 94–99 (2019). https://doi.org/10.1080/14328917.2017.1391456
73. V. Parol, A.N. Prabhu, M.A. Taher, S.R.G. Naraharisetty, N.K. Lokanath, V. Upadhyaya, A third-order nonlinear optical single crystal of 3,4-dimethoxy-substituted chalcone derivative with high laser damage threshold value: a potential material for optical power limiting. J. Mater. Sci.

Mater. Electron. **31**, 9133–9150 (2020). https://doi.org/10.1007/s10854-020-03443-2

74. B. Sahaya Infant Lasalle, A. Manikandan, M. Senthil Pandian, P. Ramasamy, Theoretical and experimental investigation on 1,2,3-benzotriazole 4-hydroxybenzoic acid (BTHBA) single crystals for third-order nonlinear optical (NLO) applications. Cryst. Res. Technol. **58**, 2200155 (2023). https://doi.org/10.1002/crat.202200155
75. A.U. Habeeba, M. Saravanan, T.S. Girisun, S. Anandan, Nonlinear optical studies of conjugated organic dyes for optical limiting applications. J. Mol. Struct. **1240**, 130559 (2021). https://doi.org/10.1016/j.molstruc.2021.130559
76. K. Prathebha, K. Raju, T.A. Hegde, G. Vinitha, Computation and experimental results on spectroscopic and physicochemical properties of efficient piperidine driven passive optical limiting material. Phys. Scr. **97**, 035804 (2022). https://doi.org/10.1088/1402-4896/ac4d00
77. N. Kobko, A. Masunov, S. Tretiak, Calculations of the third-order nonlinear optical responses in push–pull chromophores with a time-dependent density functional theory. Chem. Phys. Lett. **392**, 444–451 (2004). https://doi.org/10.1016/j.cplett.2004.05.078
78. S.R. Marder, D.N. Beratan, L.T. Cheng, Approaches for optimizing the first electronic hyperpolarizability of conjugated organic molecules. Science **252**, 103–106 (1991). https://doi.org/10.1126/science.252.5002.103
79. A.J. Almosawe, H.L. Saadon, Nonlinear optical and optical limiting properties of new structures of organic nonlinear optical materials for photonic applications. Chin. Opt. Lett. **11**, 041902 (2013). https://doi.org/10.3788/COL201311.041902
80. S. Tretiak, V. Chernyak, Resonant nonlinear polarizabilities in the time-dependent density functional theory. J. Chem. Phys. **119**, 8809–8823 (2003). https://doi.org/10.1063/1.1614240
81. M. Shkir, S. AlFaify, M. Arora, V. Ganesh, H. Abbas, I.S. Yahia, A first principles study of key electronic, optical, second and third order nonlinear optical properties of 3-(4-chlorophenyl)-1-(pyridin-3-yl) prop-2-en-1-one: a novel D-π-A type chalcone derivative. J. Comput. Electron. **17**, 9–20 (2018). https://doi.org/10.1007/s10825-017-1050-3